AN ABSTRACT OF THE THESIS OF

Ajit Sharma for the degree of Master of Science in

Electrical and Computer Engineering presented on July 31, 2003.

Title: Predictive Methodologies for Substrate Parasitic Extraction and Modeling in Heavily Doped CMOS Substrates.

Redacted for Privacy Redacted for Privacy

Abstract approved: _____ _____

Kartikeya Mayaram Terri S. Fiez

This thesis presents an automated methodology to calibrate the substrate profile for accurate prediction of substrate parasitics using Green's function based extractors. The technique requires fabrication of only a few test structures and results in an accurate three layered approximation of a heavily doped epitaxial silicon substrate. The obtained substrate resistances are accurate to about 10% of measurements. Advantages and limitations of several common measurement techniques used to measure substrate z-parameters and resistances are discussed. A new and accurate z-parameter based macro-model has been developed that can be used up to a few GHz for P^+ contacts that are as close as $2\mu m$. This enhanced model also addresses the limitations of previous models with regards to implementation aspects and ease of integration in a CAD framework. Limitations of this modeling approach have been investigated. The calibration methodology can be used along with the scalable macromodel for a qualitative pre-design and pre-layout estimation of the digital switching noise that couples though the substrate to sensitive analog/RF circuits.

Predictive Methodologies for Substrate Parasitic Extraction and Modeling in Heavily Doped CMOS Substrates

by

Ajit Sharma

A THESIS

submitted to

Oregon State University

in partial fulfillment of
the requirements for the
degree of

Master of Science

Completed July 31, 2003
Commencement June 2004

Master of Science thesis of Ajit Sharma presented on July 31, 2003

APPROVED:

Redacted for Privacy

Co-Major Professor, representing Electrical and Computer Engineering

Redacted for Privacy

Co-Major Professor, representing Electrical and Computer Engineering

Redacted for Privacy

Director of the School of Electrical Engineering and Computer Science

Redacted for Privacy

Dean of the Graduate School

I understand that my thesis will become part of the permanent collection of Oregon State University libraries. My signature below authorizes release of my thesis to any reader upon request.

Redacted for Privacy

Ajit Sharma, Author

ACKNOWLEDGEMENT

Let me begin by thanking my advisors Dr. Karti Mayaram and Dr. Terri Fiez. They both have, with their thought-provoking observations, enabled me to think independently. Their pointed questions kept me forever questioning my premise and thus honing my knowledge. My interest in modeling and Design Automation stemmed primarily from Karti's inspirational class on Analog Circuit Simulation. What I have learned from my advisors, I am sure, will serve me in good stead in my future research and I consider myself extremely fortunate to have worked with them.

I would also like to acknowledge Dr. Chenggang Xu and Dr. Lewis Semprini, for showing interest in my work and serving on my defense committee. Thanks to Dr. Semprini for taking time off his busy schedule!

I would like to thank NSF, SRC and DARPA for sponsoring this project.

I would like to thank Dr. Nishath Verghese and Dr. Wen Kung Chu from Cadence Design Systems for many helpful discussions and their help with matters relating to both modeling and parasitic extraction.

I also thank Ferne Simendinger, April Melton and Sarah O'Leary for all their help and co-operation during my schooling at OSU.

I am also grateful to Dr. Ashok Nedungadi from MicroSystems Engineering Inc./Biotronik Inc. for a chance to intern at Micro Systems Engineering during the summer of 2002. I really learned a lot from him technically and am grateful to him for giving me a whole new insight into the world of analog design.

Thanks to the entire subtrate coupling group. Time spent with them is going to be a chunk of my nostalgic memories of OSU. I am greatly thankful to Shu-Ching

Hsu, Husni Habal, Patrick Birrer, Brian Owens and Sirisha for all the help and cooperation on the substrate coupling project over the last two years. Thanks also to HuiEn Pham, Scott Hazenboom, Sasi Kumar Arunachalam, Prasad Talasila and Martin Held and all the best to them.

I thank Neel and Sachin for their help guidance during the initial phase of my life here at Corvallis. I thank Robert Batten, Paul Hutchinson and James Ayers for all the thoughful discussions regarding measurements. Many thanks are also due to Taras, Vova, Michael Kelm and Chenggang for helping me with technical problems - both with substrate coupling and optmization. Thanks also to Alexey Malishevsky for all his help with LaTeX.

I remain thankful to my friends Ranganathan, Rajarajan, Sachin, Ravikanth, Kannan, Madhu, Nathen, Prashanth, KP, Mohana, Trimmy, Vinay, Sharath, Nimish, Shuba, Gautham, Vivek, Pavan, Manas, Manu, Laddu, Triet, YuHua Guo, Zhimin Li and Ashok for helping me out in myriad ways during my stay here in the US.

Many thanks to Taras, Patrick and Vova for being such great company during my two years here at OSU. Friends like them are hard to come by.

If there is anybody who is responsible for helping me make it this far in life, it is those two people whom I call Mummy and Daddy. Needless to mention, words are inadequete to express the gratitude I feel for them. They have been a pillar of strength and inspiration and I owe my success to them. I wish to thank Madhura and Amit Nayyar for all their encouragement and support, which have gone a long way in helping me complete my Masters.

And above all, I thank God for everything.

TABLE OF CONTENTS

TABLE OF CONTENTS (Continued)

TABLE OF CONTENTS (Continued)

Page

LIST OF FIGURES

LIST OF FIGURES (Continued)

Figure | Page

LIST OF FIGURES (Continued)

Figure | Page

Figure Page

LIST OF TABLES

To my Parents

PREDICTIVE METHODOLOGIES FOR SUBSTRATE PARASITIC EXTRACTION AND MODELING IN HEAVILY DOPED CMOS SUBSTRATES

1. INTRODUCTION

1.1. Introduction

The last decade has seen the so-called wireless revolution and this has been made possible by advances in the areas of integrated circuit (IC) design and electronic design automation (EDA). With low-cost, low-power and high-speed being the motto of this revolution, a System-on-a-Chip (SoC) was the proposed solution.

However, there are numerous problems that must be tackled - especially those concerning the practical implementation of such systems. Only then, can SoC solutions be applied to a wide range of customer specific problems, e.g. those systems that operate at radio frequencies (RF).

Complementary metal-oxide semiconductor (CMOS) technology is very attractive for analog and mixed-signal applications because of the potential packing density and power savings it can offer. This has made CMOS the workhorse of modern digital VLSI circuits. CMOS technology, however, is still in its infancy when it comes to large mixed-signal and RF applications. This is because of the increased amounts of digital switching noise generated from the digital portions of these chips. This switching noise tends to increase with reduced feature sizes and increasing clock frequencies. Digital switching noise that couples from the digital

blocks to sensitive analog blocks on the same chip, via the shared silicon substrate is often referred to as *substrate noise*. Figure 1.1 illustrates the general substrate noise coupling problem. The main aspects are highlighted - generation at the digital end, propagation through the common silicon substrate and finally the pickup and its impact on sensitive analog circuitry.

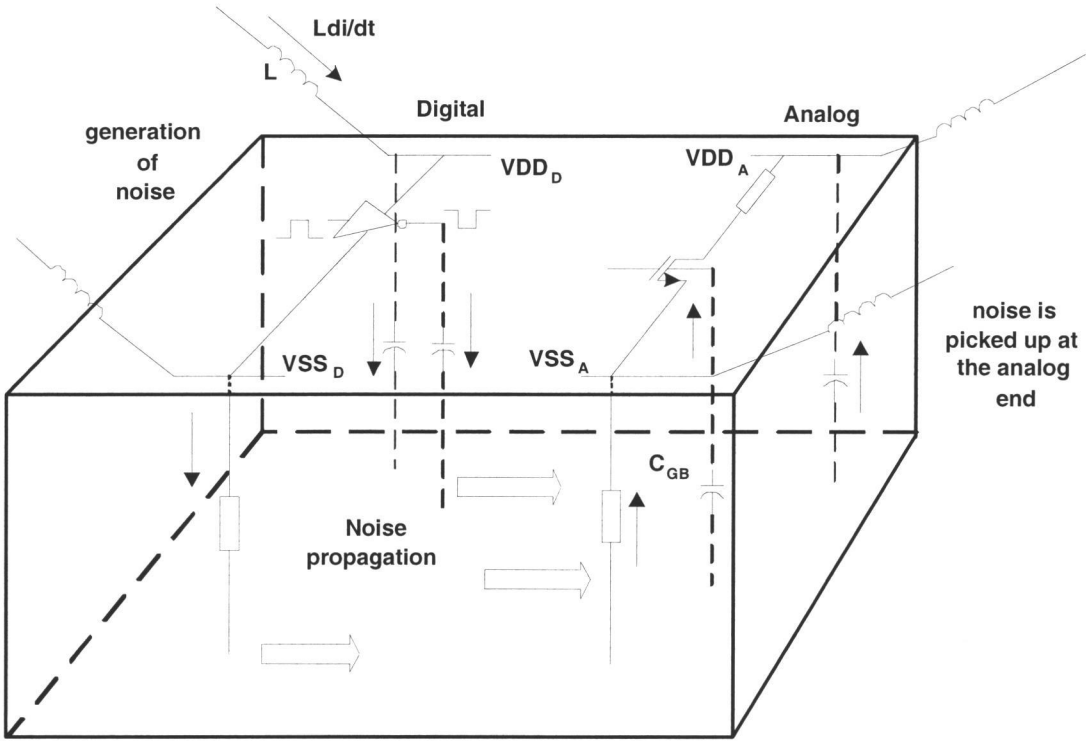

Figure 1.1. The general substrate noise coupling problem showing injection by a digital block, propagation though the silicon substrate and pickup by a sensitive analog block.

1.2. Motivation

Substrate noise coupling is becoming increasingly important in present day mixed-signal SoC designs. As shown in Figure 1.1, digital switching nodes are capacitively coupled to the substrate through either junction capacitances or through interconnect/bond-pad capacitances. This causes voltage variations in the underlying substrate, which leads to a current pulse flowing from the switching node to the substrate taps. As this current pulse propagates through the substrate, it causes a potential fluctuation in the substrate voltage of the underlying transistors that lie in its path. This can affect circuit performance through the body effect.

The threshold voltage(V_t) of an NMOS transistor is given by,

$$V_t = V_{t0} + \gamma(\sqrt{2\Phi_F + V_{SB}} - \sqrt{2\Phi_F}) \tag{1.1}$$

where V_{SB} is the source to body voltage, V_{t0} is the zero bias threshold voltage, Φ_F is the Fermi level and γ is the body effect parameter. As can be seen from Eq. (1.1), fluctuation of the body potential will lead to changes in V_{SB}, thus causing a change in the threshold voltage. The drain current of a transistor is given by:

$$I_D(lin) = k_n' \frac{W}{L} \left\{ (V_{GS} - V_t)V_{DS} - \frac{1}{2}V_{DS}^2 \right\} \{1 + \lambda V_{DS}\} \tag{1.2}$$

$$I_D(sat) = \frac{k_n'}{2} \frac{W}{L} (V_{GS} - V_t)^2 (1 + \lambda V_{DS}) \tag{1.3}$$

for the linear and saturation regions, respectively. As these depend on the threshold voltage V_t, fluctuations in the transistor body potential directly lead to noisy drain currents.

Substrate noise manifests itself in various forms depending on the circuit. As explained above, substrate noise can couple to the drain current of transistors,

mixing with the signal of interest and thereby degrading the noise performance of the whole system. Substrate noise causes an increase in the phase noise and jitter of oscillators and a degradation of the noise figure in low noise amplifiers (LNAs).

The DC components of the substrate potentials can cause a change in the depletion capacitances that exist between the devices and the substrate. If a device-substrate capacitance gets forward biased due to a large voltage spike, a large current gets injected into the substrate and this can lead to permanent damage of the IC [1].

Over the last couple of years there has been considerable emphasis on solving issues related to electro-static discharge (ESD), latch-up and power aware synthesis. To make SoC solutions a reality, substrate noise coupling must be added to this list. Substrate noise coupling analysis must, hence, be integrated into a standard design flow and made as seamless as a design rule check (DRC), layout-vs-schematic (LVS), or parasitic extraction - analyses that are very much part of any standard design flow.

Substrate noise coupling has been a difficult problem to tackle owing to the number of parameters that can vary. Therefore, one approach to the problem is the use of numerical methods to model the substrate [2, 3]. These, however, would be slow for large systems and are not convenient for estimation purposes. During the initial stages of design of mixed-signal circuits, designers are interested primarily in obtaining a qualitative idea about the amount of coupling between various blocks. The exact numerical values of the underlying substrate parasitics are not critical and a certain amount of accuracy can be sacrificed depending on the stage of design.

A simple equation that relates key parameters of the substrate and can easily be adapted to the design problem at hand will aid a designer considerably in design decisions. This equation can offer more insight into the behavior of the substrate as a collector and distributor of noise, than a set of differential equations that need to be solved numerically.

It is with a view to obtaining such equations that empirical methodologies have been proposed in [4–6] to model the substrate.

1.3. Previous work

As mentioned earlier, considerable work has been done in modeling the substrate. The methods employed currently to model the substrate are listed below:

1. Finite difference method [7], [8].
2. Boundary element method (BEM) [3], [9].
3. Pre-processed boundary element method [2].
4. Scalable macro-model [4], [5], [6].

A detailed description of the various methods can be obtained from the appropriate references. Another comprehensive source for the various methods is [10].

1.4. Contribution of this work

The use of scalable macro-models for the silicon substrate is gaining popularity as an effective and quick means of determining, a-priori, the amount of digital

switching noise that couples from digital portions of the chip to the sensitive analog portions [4, 5, 11]. However, the limitations of such an approach are:

(i) Existing macro-models address separations only greater than $10\mu m$ [13]. In a practical layout, circuit blocks (e.g. substrate taps adjacent to transistors) are situated at separations as close as $2 - 5\mu m$.

(ii) Existing models [5] use geometry dependent parameters that can be ambiguous. Hence these methods are not directly amenable for implementation in a CAD framework.

(iii) There is a lack of a formal methodology to extract these models. Process data from a foundry must be used to determine the substrate resistances for an arbitrary set of substrate contacts of interest.

(iv) Finally, these approaches cannot be used in regions where the substrate contacts of interest are so close that proximity effects become important. Hence, a possible extension of this macro-modeling approach has been suggested which involves the discretization of the larger substrate contacts into panels.

In this thesis, the emphasis has been on developing a model and an accompanying methodology for parameter extraction. The model can be integrated into a tool to address the problem of accurately modeling the substrate parasitics and thereby the noise propagation through the substrate.

Additionally, an automated methodology to calibrate the substrate profile for use with substrate parasitic extractors based on the Green's function approach [3, 9] has been developed. This results in a simple 3-layered representation of the substrate, which when used with Green's functions based extractors yields accurate values of substrate resistances. A heavily doped substrate with an epitaxial layer

has been used as a platform for the development of this methodology and for the development of an improved z-parameter based macro-model for the substrate parasitics. Though z-parameters have been modeled earlier in the pre-processed BEM [2] using curve fitting techniques, the emphasis in this work has been on deriving simple equations that can give the designer a better understanding of the nature of the noise propagation. This model is an enhancement of that presented in [4] or [5] in that it is applicable over a wider range of separations. It uses an approach that lends itself to easy implementation in a CAD framework. This is because it makes use of unambiguous geometry dependent parameters.

Finally the calibration, model extraction and validation methodologies described have been integrated into a Comprehensive Automated Substrate Parasitic Extraction Routine (CASPER).

1.5. Thesis outline

Chapter 1 is an introduction to the substrate noise coupling problem and the motivation for this work and its scope. Chapter 2 describes the measurement procedure. Chapter 3 outlines the need for an automated methodology for the calibration of the substrate profile for use with Green's function based substrate parasitic extractors, presents the calibration methodology and validates this calibration against measured data. The rationale behind the model development and the scalable 3-D model for epi-type substrates is presented in Chapter 4. Chapter 5 presents validation results as applied to an arbitrary test case of multiple contacts and finally conclusions are drawn in Chapter 6. This work, can by no means, completely ad-

dress the substrate noise coupling issue and possible future research avenues are also included in Chapter 6.

2. MEASUREMENT TECHNIQUES

The measurements to validate the results described in this work were made on P^+ test structures fabricated in the $0.35\mu m$ CMOS (heavily doped epitaxial) TSMC process through MOSIS. The die photograph is shown in Figure 2.1. All

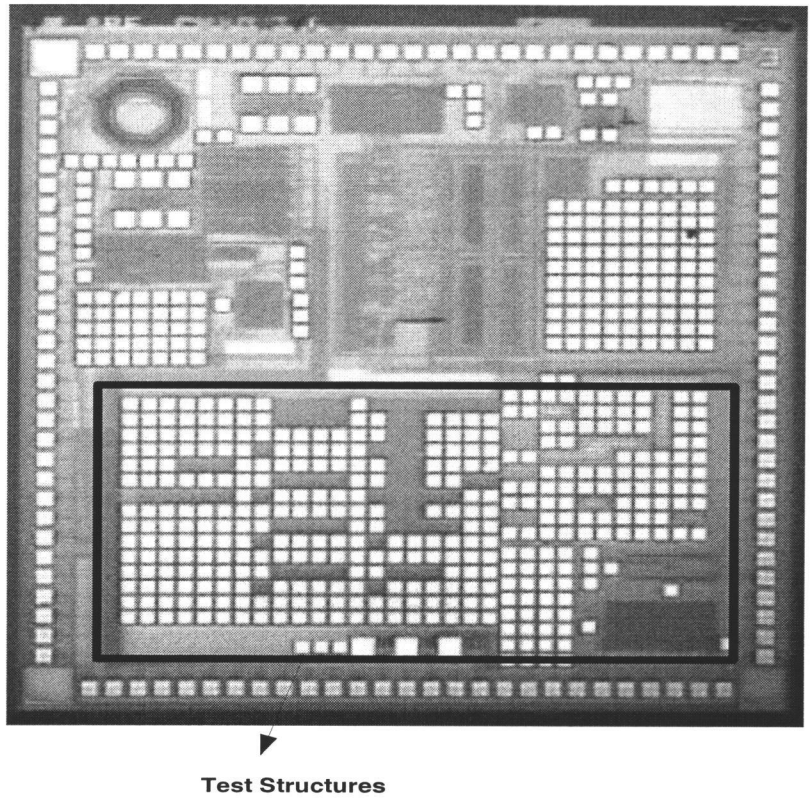

Figure 2.1. Die photograph of the test chip fabricated in the $0.35\mu m$ CMOS TSMC heavily doped epitaxial process.

test structures were connected to $70\mu m$ x $70\mu m$ DC probe pads for probing. A description of the test structures has been provided in Appendix B. The measurement

set-up consists of an HP 4156B semiconductor parameter analyzer and a CASCADE probe station.

The chapter begins with an introduction to z-parameters and their relationship to the parasitic resistances between two substrate contacts. The above-mentioned methodology as well as the future macro-model are based on these open-circuit z-parameters. Then the relevance of the back-plane in heavily doped substrates has been explained in this chapter. This is followed by a comparison of three different measurement procedures. Finally conclusions based on these results have been presented, which offer an insight into the mechanism of substrate noise propagation in heavily doped substrates.

2.1. Z-parameters and substrate resistances

The inherent advantage of developing a model based on the open-circuit parameters (or z-parameters) instead of one based on the short-circuit parameters (y-parameters) is that the former can account for the case of multiple contacts in 3 dimensions [13].

For a simple two-port problem, as shown in Figure 2.2, the z-parameter representation is given by:

$$V_1 = Z_{11} I_1 + Z_{12} I_2 \tag{2.1}$$

$$V_2 = Z_{21} I_1 + Z_{22} I_2 \tag{2.2}$$

The z-parameters are expressed in terms of a single voltage and current by setting either $I_1 = 0$ or $I_2 = 0$, i.e., by forcing a current though one port and measuring the voltage at the other port which is an open circuit.

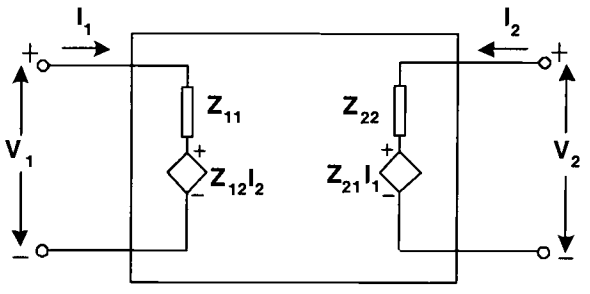

Figure 2.2. The z-parameter representation of a two-port system.

$$Z_{11} = \left(\frac{V_1}{I_1}\right)_{I_2=0}, \quad Z_{12} = \left(\frac{V_1}{I_2}\right)_{I_1=0}, Z_{21} = \left(\frac{V_2}{I_1}\right)_{I_2=0}, Z_{22} = \left(\frac{V_2}{I_2}\right)_{I_2=0}. \quad (2.3)$$

For a reciprocal network $Z_{12} = Z_{21}$.

The substrate can be modeled as in [4, 6, 13] by a simple π-network of resistances. Between two ports[1] of interest there is a cross coupling resistance, R_{12}, and resistances R_{11} and R_{22} from each of the ports to the back-plane.

Figure 2.3 shows the π-resistive network and Eqs. (2.4) and (2.5) give the relationship between the resistance values and the equivalent z-parameters. Here a current I_1 is injected into the substrate at port 1, and port 2 is left open. From

---

[1] A P^+ diffusion region on the substrate is referred to as a P^+ contact, or *port*. Henceforth in this thesis the terms port or P^+ contact will be used inter-changeably and refer to the same physical structure. Examples of ports in real circuits are substrate taps and active regions of transistors.

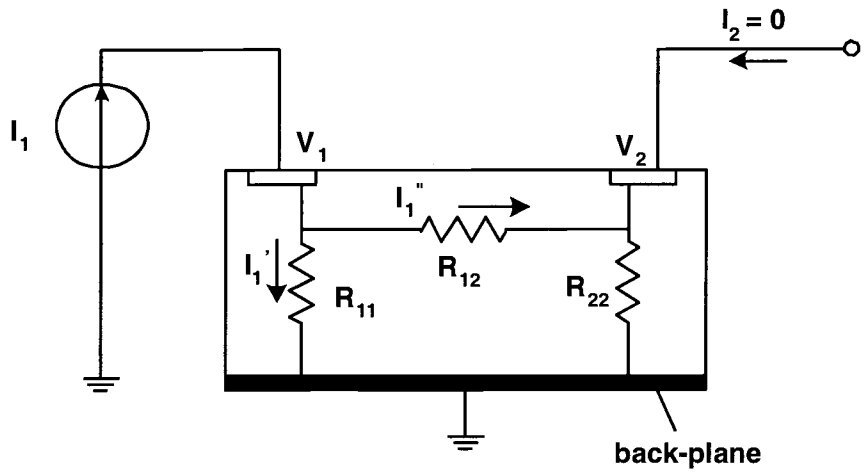

Figure 2.3. The π resistance network for the substrate parasitics between two ports.

simple circuit theory and application of Kirchoff's laws to the network shown in Figure 2.3:

$$Z_{11} = R_{11} I_1' = R_{11} \parallel (R_{12} + R_{22}) \tag{2.4}$$

$$Z_{12} = R_{22} I_1'' = \frac{R_{11} R_{22}}{R_{11} + R_{12} + R_{22}} \tag{2.5}$$

The above equations have been derived for a case where the back-plane has been grounded. When the back-plane is left floating, the resistance seen between the two ports is the parallel combination of R_{12} and $(R_{11} + R_{22})$. This resistance is denoted by R_P, and is given by:

$$R_P = R_{12} \| (R_{11} + R_{22}) = \frac{R_{12}(R_{11} + R_{22})}{R_{11} + R_{12} + R_{22}} \tag{2.6}$$

2.2. The back-plane and its relevance in heavily doped substrates

The z-parameters must be measured with respect to a reference node, which in our case is the back-plane. The "back-plane" refers to the physical back side of the die. In heavily doped substrates, it is a common practice to silence the "bulk" node by grounding the back-plane [19, 11]. In some cases, the back-side of the die can be connected to a metal plate via a conductive epoxy [4]. In this case,the inductance at the back-plane node due to the bond-wire and the epoxy (if used) must be tuned out with a suitable tuning scheme [3, 19] to prevent voltage bounces at the back-plane.

To provide a connection to the back-plane, in the test chip described above, a grounded P^+ guard ring around the perimeter of the die was used. This die-perimeter ring has been found to be an effective means of grounding the back-plane [11] in heavily doped substrates. The die-perimeter ring was connected to a pin though a bondwire, and also to a DC probe pad for probing. The measurements in this thesis were made by probing the on-chip die-perimeter ring pad.

As shown in Figure 2.4, there is a small resistance, R_{BP_DP}, between the actual back side of the die and the die-perimeter ring contact that is probed. This resistance, albeit small, significantly influences the measured values of the substrate resistances and its effect must, therefore, be removed.

The measured resistance between the actual back-plane and the die perimeter ring contact was found to be of the order of 1.5 - 3 Ω, and dominated by the contact spreading resistance of the die-perimeter ring pad. The de-embedding of this resistance from measurement data is described in Appendix C.

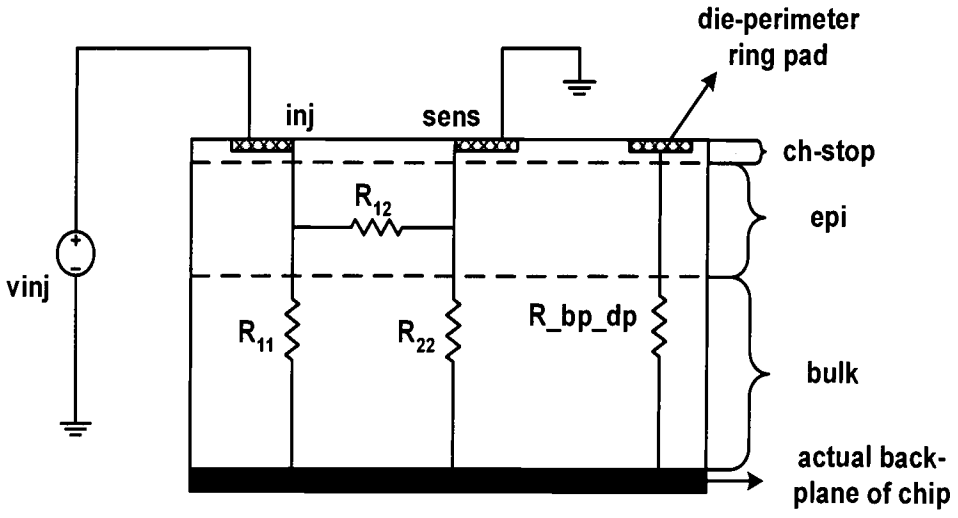

Figure 2.4. Cross section of the heavily doped substrate showing the resistance between the actual back-plane and the die-perimeter ring contact.

2.3. Measurement procedures

This section outlines three different measurement techniques that were used to measure the two port z-parameters. Each method approaches the problem from a different angle, but all must yield the same results in accordance with theory. For these measurements, if a particular port was to be left floating, a small current[2] (usually in the order of 1 - 10 nA) was forced into it and the voltage was measured.

---

[2]This current must be at least a couple of orders of magnitude smaller than the currents that are being injected or sensed.

2.3.1. Direct measurement of z-parameters

By definition, the z-parameters are open circuit parameters (Eq.(2.3)) and are obtained by injecting a current into one port (say I_{inj}), and measuring the voltage at the second port (V_{sens}). Exactly the same procedure can be used to measure the z-parameters on silicon as shown in Figure 2.5. Probe 3 and Probe 2 are used to force the current I_{inj} and sense the voltage V_{sens} at the injector and sensor, respectively. Probe 1 is used to ground the back-plane, by grounding the die-perimeter ring contact as explained in Section 2.1. Probe 4, is placed on the die-perimeter ring probe-pad as well and left floating.

An initial measurement[3] involving only probes 4 and 1 yields the value of the die-perimeter ring contact resistance. A small value of the contact resistance indicates a good back-plane connection.

The voltage at the die-perimeter ring pad is not exactly zero (though the probe is grounded) due to the parasitic resistances of the probe. Probe 4 is left floating after the initial contact resistance measurement. It serves to measure the small voltage at the die-perimeter ring probe pad. This voltage (V_{BP}) is used in de-embedding the finite back-plane and bulk resistances as described in Appendix C.

The z-parameters are calculated as follows:

$$Z_{11} = \frac{V_{inj} - V_{BP}}{I_{inj}} \tag{2.7}$$

---

[3]The switch on probe 4 indicates that the entire measurement is a two-step procedure

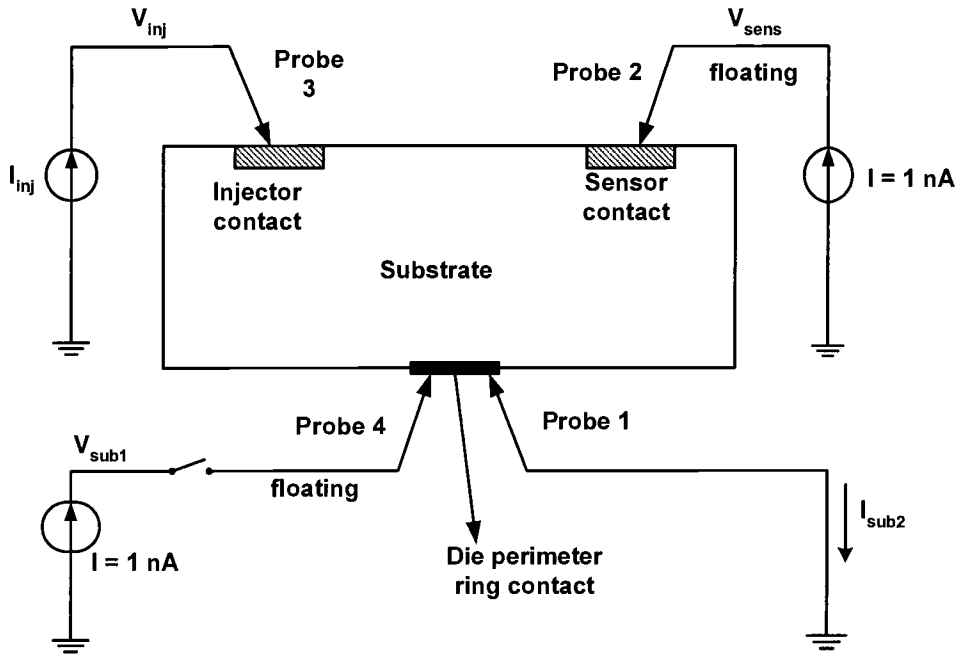

Figure 2.5. Measurement set-up for directly measuring z-parameters. Note that the back-plane is grounded to serve as a reference node.

$$Z_{12} = \frac{V_{sens} - V_{BP}}{I_{inj}} \tag{2.8}$$

where V_{inj} and V_{sens} are the voltages at the injector and sensor ports; I_{inj} and I_{sens} are the currents through the injector and sensor probes respectively and V_{BP} is the voltage at the back plane.

As mentioned earlier, the z-parameters must be measured with respect to a reference node - the back-plane in this case. It is interesting to note what happens in the above set-up when the back-plane is left floating. Port 2 that has been left floating provides no path for the current to flow, and hence the voltage at node 2 cannot be determined as shown in Figure 2.6. Hence the two-port z-parameters cannot be measured without a reference node.

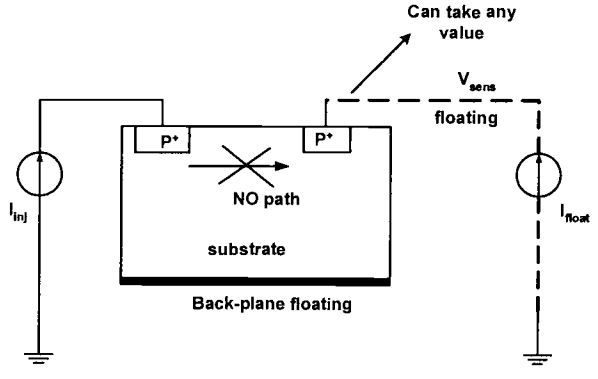

Figure 2.6. Voltage at port 2 cannot be determined when the back-plane is left floating as the circuit is not complete and there is no path for current flow.

When the back-plane is floating, the system essentially reduces to a one-port network, as shown in Figure 2.7. A one-port system is uniquely characterized by its self-impedance, Z_{ii}, and measurement of this parameter calls for the set-up shown in Figure 2.7. In this case, the Z_{ii} is given by

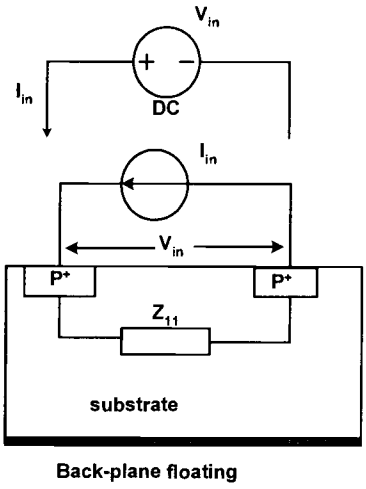

Figure 2.7. Measurement setup for a one-port system.

$$Z_{ii} = \frac{V_{in}}{I_{in}} \tag{2.9}$$

For a one-port, there are only two terminals and it does not matter whether a voltage or a current is forced for the measurements.

Though this direct method of measuring the two-port z-parameters (with the back-plane grounded) may seem accurate and very simple, it has important limitations. These limitations have to do with the resolution of the voltage and current measuring equipment used. This issue is addressed in greater detail in Section 2.4.

2.3.2. Measurement of z-parameters with the back-plane floating

An alternate method of determining the z-parameters from measurements has been outlined in [21]. This method solves the issue of parasitics dominating the measurement set-up at large separations. Additionally, no back-plane connection is required and equivalent deductions for the network in Figure 2.3 are made from measurements of a chip that has the back-plane floating. A pilot measurement is done for a case where the contacts are sufficiently far apart to determine Z_{ii}. [19] suggests that this distance be at least 4 times the thickness of the epitaxial layer ($4t_{epi}$). This case corresponds to the one-port discussed earlier (Figure 2.7). Here the Z_{ii} of the one-port is equal to the sum of the resistances from each individual contact to the back-plane, as shown in Figure 2.8.

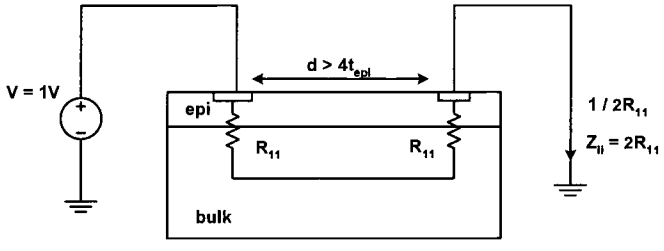

Figure 2.8. Determining Z_{ii} with the back-plane floating.

When the contacts are closer to each other (the distance separating them is less than 4 times the thickness of the epitaxial layer, and denoted as $4t_{epi}$ in the figure), the cross resistance between them cannot be ignored and the network is as shown in Figure 2.9. The Z_{12} is then calculated as described next.

Assuming the contacts are identical, Eqs. (2.4), (2.5) and (2.6) reduce to:

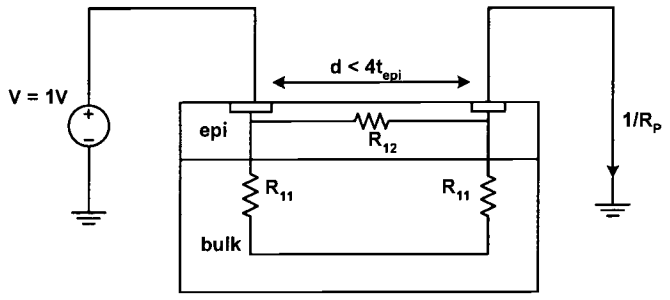

Figure 2.9. Determining Z_{ij} with the back-plane floating for identical contacts.

$$Z_{11} = R_{11} \parallel (R_{12} + R_{11}) \tag{2.10}$$

$$Z_{12} = \frac{R_{11}^2}{2R_{11} + R_{12}} \tag{2.11}$$

$$R_P = 2R_{11} \parallel R_{12} \tag{2.12}$$

Let $(2R_{11} + R_{12}) = P$, and solve for P from Eqs. (2.10) and (2.12). This yields two values for P.

$$P = \frac{R_{11}R_{12} + R_{11}^2}{Z_{11}} \tag{2.13}$$

$$P = \frac{2R_{11}R_{12}}{R_P} \tag{2.14}$$

Equating (2.13) and (2.14) and solving,

$$\frac{Z_{11}}{R_P} = \frac{R_{11}\left(R_{12} + R_{11}\right)}{2R_{11}R_{12}} = \frac{1}{2}\left(1 + \frac{R_{11}}{R_{12}}\right) = \frac{1}{2} + \frac{R_{11}}{2R_{12}} \tag{2.15}$$

Therefore,

$$\frac{Z_{12}}{R_P} = \frac{R_{11}}{2R_{12}} = \frac{Z_{11}}{R_P} - \frac{1}{2} \tag{2.16}$$

or

$$Z_{12} = Z_{11} - \frac{1}{2}R_P \tag{2.17}$$

Thus after making the pilot measurement to determine Z_{ii}, the values of Z_{12} can be calculated from a measurement of R_P.

The main disadvantages of this method, however, are:

(i) This method assumes a constant Z_{ii}, that is independent of separation. Though this may be true for small sized contacts, it is not a valid assumption for large contacts at small separations. This is further explained in Chapter 5.

(ii) This method assumes an a-priori knowledge of the separation "$4t_{epi}$", that corresponds to 4 times the thickness of the epitaxial region, beyond which R_{12} can be neglected. Beyond a certain separation (here $4t_{epi}$), the cross resistance R_{12} between the ports becomes large and the current flows vertically though the epitaxial layer, through the heavily doped bulk and then up through the epitaxial layer to the sensor [4, 19]. Hence, a designer needs to know the separation between the substrate ports, beyond which R_{12} can be neglected.

For the measurements in this thesis, the z-parameters were calculated from admittance measurements made between the substrate ports. The measurements were taken with the back-plane grounded.

2.3.3. Determination of z-parameters from equivalent admittance measurements

The value of Z_{ii}, or the z-parameter from the contact to the back-plane was assumed constant in the previous analyses. However it has been observed that for large contacts (larger than $10\mu m \times 10\mu m$) at small separations (less than $10\mu m$), this assumption is no longer valid. This can be attributed to the fact that at small separations proximity effects become significant and hence the value of Z_{ii} changes[4].

In heavily doped substrates, a method to reduce noise coupling is to ground the back-plane [19]. This is very effective in reducing the overall noise that can couple through the substrate, as has also been shown in [11] as well. Since ICs that use heavily doped substrates usually have a means for grounding the back-plane, it is worthwhile to investigate a reliable measurement method for the z-parameters given that the back-plane is grounded.

The set-up used to perform the measurements has been shown in Figure 2.10. The main difference between Figures 2.5 and 2.10 is that in the former, a current is injected and a voltage is measured (at a port which is an open-circuit), while in the latter a voltage is forced at a port and a current is measured (though a port that is a short circuit). In Figure 2.10, the voltage V_{inj} is applied at the injector using Probe 3, and Probe 2 at the sensor is grounded (compare this to the set up in

---

[4]This must be noted carefully because the so-called "self-impedance", Z_{ii}, of the port is now dependent on other contacts in its immediate vicinity. As the value of Z_{ii} depends on its relative location to other contacts, it can no longer be referred to as the "self-impedance."

Figure 2.5). As in Figure 2.5, Probe 1 is used to ground the back-plane, by grounding the die-perimeter ring contact as explained in Section 2.1. Probe 4, is placed on the die-perimeter ring probe-pad as well. Again, as explained in Section 2.1, the measurement is a two-step procedure where the initial measurement involving only probes 4 and 1 yields the value of the contact resistance. Subsequently, probe 4 is left floating to measure the back-plane voltage, as explained earlier. Hence, the measurement set up described here measures an admittance rather than the z-parameters.

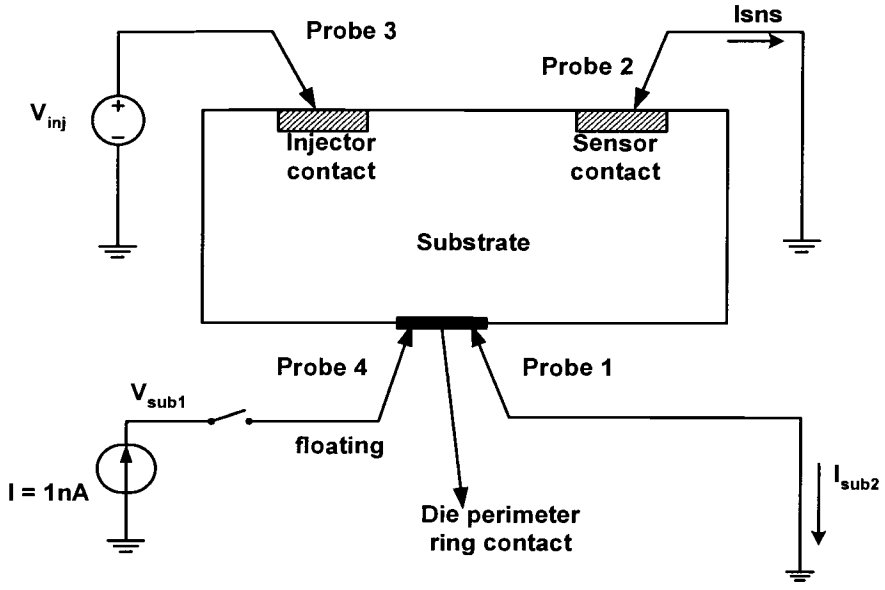

Figure 2.10. Measurement set up for measuring admittances with the back-plane grounded.

After de-embedding the die-perimeter ring to the back-plane resistance (Appendix C), R_{DP-BP}, we get the values of the resistances as:

$$R_{11} = \frac{V_{inj} - V_{sub1}}{I_{sub2}} \tag{2.18}$$

$$R_{12} = \frac{V_{inj} R_{11}}{R_{11} I_{inj} - V_{inj} + V_{sub1}} \tag{2.19}$$

2.4. Measurement results

Figure 2.11 compares the Z_{12} values obtained from direct measurement with those calculated from the equivalent admittance measurements, for two contact sizes. As can be seen, the direct and indirect admittance based measurements are in good

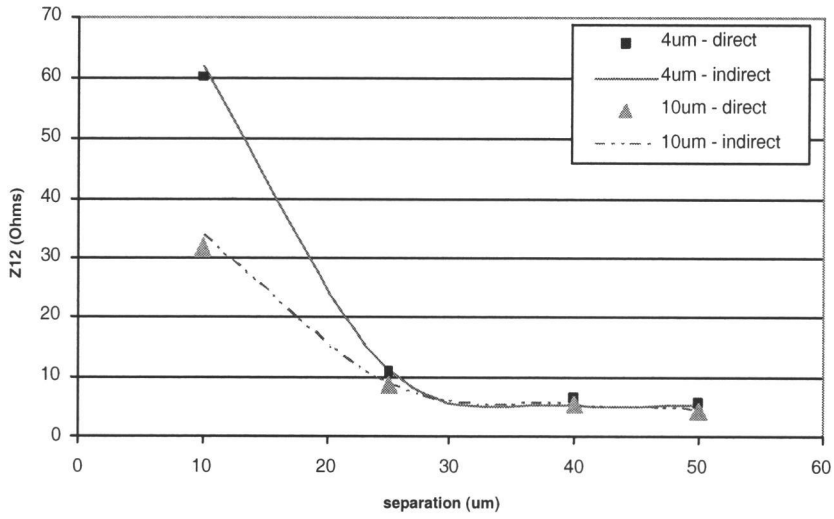

Figure 2.11. Z_{12} measured directly matches the values obtained from the equivalent admittance measurements for $4\mu m \times 4\mu m$ and $10\mu m \times 10\mu m$ contacts.

agreement. This proves that the z-parameters for a 2-port network can be easily obtained from suitable admittance measurements.

Table 2.1. Z_{12} values obtained from direct measurements are in good agreement with those calculated from the equivalent admittance measurements. This shows that either method can be used to obtain the z-parameters.

Contact Size ($\mu m \times \mu m$)	*Separation* (μm)	Z_{12} (Ω) *Direct measurement*	$Z_{12}(\Omega)$ *From admittances*
4×4	10	60.077	61.886
4×4	25	10.778	11.258
4×4	40	6.473	5.332
4×4	50	5.577	5.465
10×10	10	31.850	33.672
10×10	25	8.551	8.724
10×10	40	5.492	5.550
10×10	50	4.425	4.374

As mentioned earlier, the direct measurement of z-parameters is limited by the minimum voltage resolution of the measuring device used in the set-up. The measurement set-up used to obtain the substrate parameters for the work described in this thesis consisted of an Agilent 4156B Precision Semiconductor Parameter Analyzer [17]. The semiconductor parameter analyzer has 4 high resolution medium power source monitor units (SMUs). The minimum current resolution of the SMUs is $1fA$, while the minimum voltage resolution is only $2\mu V$. The minimum current that can be measured is orders of magnitude smaller than the minimum measurable voltage. It is, therefore, possible to measure a much smaller short-circuit current rather than an open-circuit voltage of relatively similar magnitude.

As the admittance measurement method measures the short-circuit current, it is better suited to measuring larger R_{12}'s and hence smaller Z_{12}'s. Based on

these considerations, for measurement results in this thesis, the z-parameters were obtained using the admittance measurements.

Equivalent deductions about the total resistance between the two ports when the back-plane is floating can be made from the resistance values obtained when the back-plane is grounded. As shown in Eq. (2.6), when the back-plane is floating the resistance is the parallel combination of R_{12} and the sum of R_{11} and R_{22}. The back-plane was left floating and the total resistance between two identical ports was measured for different contact sizes. The separation between the ports was varied from $10\mu m$ to $50\mu m$. For the case of a floating back-plane only a single impedance can be determined (which happens to be the Z_{ii} of the one-port network, as explained in Section 2.2.1). The experiment was repeated with the back-plane grounded and the resistances R_{11}, R_{22} and R_{12} were determined. Using Eq. (2.6), the value of R_P was calculated. Figure 2.12 compares the measured values of Z_{ii} with the calculated values of R_P using Eq. (2.6). In the figure the darker bars represent the measured impedances (obtained when the back-plane was left floating) and the lighter ones represent the resistances calculated from measurements made when the back-plane is grounded. The taller bars are for $4\mu m \times 4\mu m$ contacts, while the shorter ones represent the $10\mu m \times 10\mu m$ contacts. The contact sizes, separations, measured impedances and the calculated resistances are tabulated in Table 2.2. As can be seen from this table, the value of the total resistance between the two ports, when the back-plane is left floating can be accurately predicted from measurements made when the back-plane is grounded.

2-D device simulations in [4] and [19] show the current flow lines in heavily doped epi-type substrates. When the substrate ports are sufficiently separated,

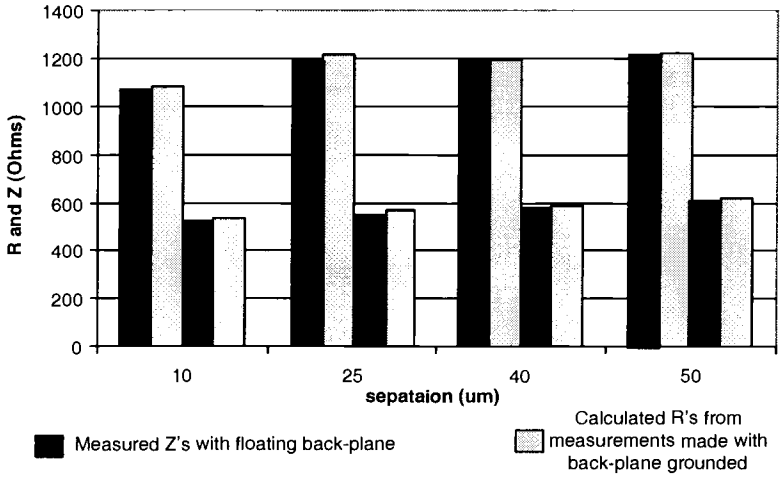

Figure 2.12. Resistances between ports when the back-plane is floating can be predicted from measurements made when the back-plane is grounded. The contact sizes are $4\mu m \times 4\mu m$ and $10\mu m \times 10\mu m$.

the injected substrate current flows down vertically through the epitaxial layer, propagates through the low resistivity bulk, and finally flows back up vertically to the sensor. 2-D device simulations in [4] also show that at separations below $10\mu m$ most of the current flow takes place though the surface. These phenomenon can be easily observed through simple measurements.

From Figure 2.9, it is seen that at close separations R_{12} cannot be neglected since it accounts for surface current propagation. In the limiting case, when the contacts are sufficiently far apart, the total resistance between them is equal to the sum of R_{11} and R_{22}. Therefore, it can be concluded that as the separation between the ports increases, the effect of R_{12} diminishes. This is evident from Figure 2.13, where the values of the parallel resistance, R_P, and $2 \times R_{11}$ (two identical

Table 2.2. The total resistance between the two ports, when the back-plane is left floating can be accurately predicted from measurements made when the back-plane is grounded.

Contact Size ($\mu m \times \mu m$)	*Separation* (μm)	$2 \times R_{ii}$ (Ω) *Direct measurement with back-plane floating*	$R_P(\Omega)$ *calculated from grounded back-plane measurements*
4×4	10	1075.633	1084.325
4×4	25	1185.749	1215.654
4×4	40	1183.334	1197.113
4×4	50	1214.308	1220.187
10×10	10	525.688	534.830
10×10	25	565.709	573.244
10×10	40	578.502	591.589
10×10	50	616.318	614.650

$0.85\mu m \times 0.7\mu m$ contacts) are plotted as a function of the separation. As the separation increases, the parallel resistance (which incidentally happens to be the Z_{ii} of the equivalent one-port network) approaches the value of $2 \times R_{11}$.

The separation at which the parallel resistance becomes approximately equal to $2R_{11}$ can be considered to be the zone beyond which the substrate noise propagation mechanism becomes predominantly bulk propagation.

2.5. Summary

Different methods to measure z-parameters have been discussed in this chapter and the merits/demerits of each have been listed. Measurements that can serve

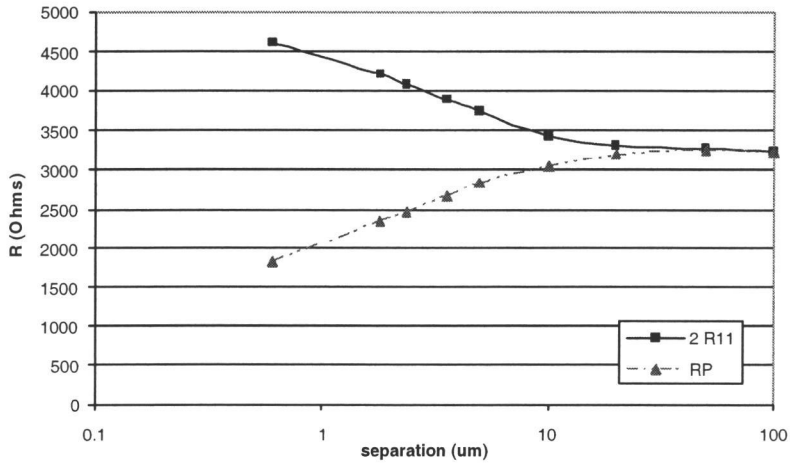

Figure 2.13. R_P and $2R_{11}$ for two $0.85\mu m \times 0.7\mu m$ contacts plotted as a function of separation. R_P must equal $2R_{11}$ for large separations.

as indicators of the accuracy of the data have been outlined. Trends previously observed from device simulations have been corroborated with measurements. These measured results along with the supporting theory bring to light the relationships between various parameters that significantly affect signal coupling between the ports of interest. This data is used for the calibration that is described in the next chapter.

3. CALIBRATION

This chapter describes an automated methodology to obtain accurate substrate parasitics from Green's function based extractors. An optimization based approach is used which enables the calibration of the substrate profile for use with such extractors. The proposed technique requires the fabrication of only a few test structures for z-parameter measurements.

The motivation for the automated calibration methodology is presented first. Then the calibration procedure is outlined and the chapter ends with the validation of the results with measurement data.

3.1. Motivation for optimization of substrate resistivities and thicknesses

3-D Green's function based substrate parasitic extractors and most commercially available substrate analysis tools (e.g., Cadence SeismIC, Agilent/EEsof-Momentum) require the substrate to be described as layers of uniform resistivities. This layered description of the silicon substrate must be derived from the actual spreading resistance profile (SRP) data of the particular process run. Typically a heavily doped substrate is approximated by a 3 layered structure and a lightly doped substrate by a 2 layered structure [3]. Therefore, the accurate determination of the equivalent resistivities and the thicknesses of the layers is important. The resistivities and thicknesses used for the layers have been found to impact the values of the extracted substrate parasitics significantly. Despite accurate SRP data, it is difficult to heuristically determine a good approximation to the substrate using only a few layers of uniform resistivities. For example, both auto doping and out diffusion can

cause the transition from the doping level of the substrate to that of the epitaxial layer to be less abrupt than desired [14].

A very fine discretization of the SRP data may yield accurate results, but the associated computational costs are enormous. For instance, if the number of layers is increased from 3 to 6 for a single injector-sensor pair, the computation time increases by about 4 times. This will result in impractical extraction times for a large number of test cases and especially if such a discretization is applied to large circuits. Therefore, this work develops an optimization based approach to obtain a simple layered description of the substrate.

The empirical macro-model introduced in Chapter 4, is extracted using a least squares data fitting methodology. The accuracy of the model, the efficiency of its extraction, and its range of application can be improved by using an optimum set of test structures. This optimum set of test structures can be obtained by developing an appropriate design of experiments (DOE). However, developing this DOE can be challenging if sufficient data is not available. In [4] and [5], z-parameter data was obtained from measurements from test structures fabricated on silicon. This can, however, be expensive and time consuming.

If an efficient and cost-effective alternative for the measurement data is available, it is possible to experiment with various sets of test structures and come up with an appropriate DOE. This would, then involve minimal dependence on fabricated test structures. It is with this objective that the use of "calibrated" Green's function based 3-D substrate parasitic extractors has been proposed. The accuracy of these extractors, as discussed earlier, depends on the layered description of the profile.

The optimization procedure proposed, uses only a few test structures to obtain optimized substrate layer resistivities and thicknesses. The Green's function based extractors can be used with these "calibrated" layer resistivities and thicknesses to obtain the z-parameters. This provides a cost-effective, reliable and fast means of obtaining the data which can then be used to develop the DOE, thus leading to a significant reduction in model development time.

In [4], the macro-model that was extracted from measured data was used to develop the resistive substrate coupling network between two circuits of interest. The optimization procedure described in this chapter can lead to reduced time for the macro-model development. Hence, this leads to the generic flow for substrate coupling analysis as shown in Figure 3.1.

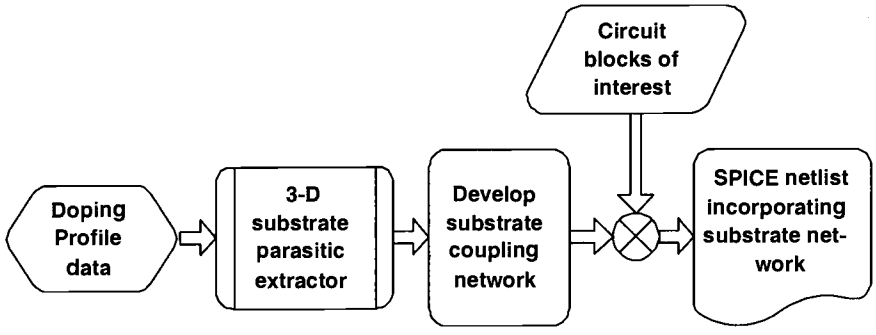

Figure 3.1. Generic flow for substrate noise analysis.

After the optimization, the resulting 3 layered approximation is accurate, as will be proved later, and speeds up computation of the substrate parasitic network significantly. The problem that the optimization routine needs to address is to be

able to suitably discretize the doping profile from the surface to the back-plane as shown in Figure 3.2.

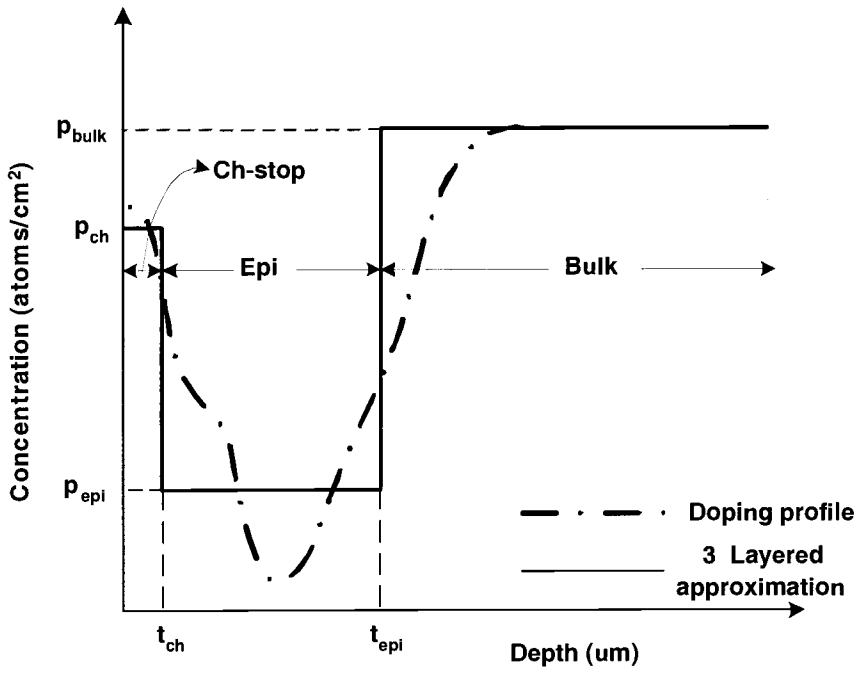

Figure 3.2. Actual doping profile and a 3 layered representation of the silicon substrate.

From a circuit design point of view, the noise transfer function (NTF) given by Eq. (3.1) is of interest.

$$\frac{v_{out}}{v_{in}} = \frac{R_{22}}{R_{12} + R_{22}} \tag{3.1}$$

As can be seen, this NTF depends on the substrate resistances. An error in the prediction of the substrate resistances will result in a corresponding error in the calculated noise voltage at the node of interest.

At this point an analogy is in order. A 3-D extractor like the one described in [9], can be compared to a circuit simulator, like SPICE. In this case, the resistivities and thicknesses of the substrate layers are inputs that can be compared to the parameters of the device models. Incorrect device model parameters are bound to lead to incorrect results, however advanced and accurate a simulation engine may be. Hence, it is important to accurately determine the proper resistivities and thicknesses.

3.2. Calibration procedure

Figure 3.3 shows the flowchart for the calibration procedure which was implemented in MATLAB. A subsequent implementation of this calibration routine in ANSI C has been developed as well. The details of the ANSI C function are given in Appendix A. The calibration procedure requires the following:

1. A fast 3-D substrate parasitic extractor.
2. An appropriate calibration metric, which depends on the substrate being calibrated.
3. An appropriate initial guess for the variables being optimized.
4. An appropriate termination criterion (e.g. tolerances on the variable values or gradients).

The Z_{11} values of eight test structures obtained from measurement are used as a reference for this calibration. These structures were fabricated on a test chip in the TSMC $0.35\mu m$ CMOS heavily doped process. The measurement methodology was

explained in Chapter 2. The set of structures chosen for calibration must span the range of equivalent port sizes that can occur in the layout. Also, since both square and rectangular ports can occur in a layout, the calibration set must include square and rectangular shaped structures as well.

3.2.1. EPIC

EPIC [9] was chosen as the 3-D Green's function based substrate parasitic extractor for the work described in this thesis. EPIC can be readily interfaced with either MATLAB or ANSI C. Hence, it could be used with MATLAB in a variety of test-benches for testing different optimization techniques. Finally, the source code was available and this made it an attractive option because future integration with other software platforms would be possible.

As was explained in Chapter 2, a P^+ guard ring was placed around the perimeter of the test chip. While obtaining measurements of Z_{11} to be used as a reference for the optimization procedure described here, the back-plane of the die was grounded by grounding this "die-perimeter" ring [11]. It was therefore necessary to include this die-perimeter ring in simulations with EPIC.

While certain Green's function based substrate parasitic extractors assume an infinite die size [16], EPIC assumes a finite die size. The die size is specified as an input by the user. The substrate ports to be analyzed must be placed inside this bounding box (which represents the die size). The actual size of the fabricated die was approximately $3000\mu m \times 3000\mu m$. However, the larger the size of the bounding box, the larger is the memory and computational time required by EPIC. Hence,

for simulations with EPIC a bounding box of $1000\mu m \times 1000\mu m$ was used. The size of the bounding box affected the values of Z_{11} only by about 2 %[1].

Further for simulations with EPIC the contacts were placed in the center of the $1000\mu m \times 1000\mu m$ bounding box for simplicity. The values of the substrate resistances were found to be in close agreement (less than 1 - 2 % variation) with those obtained when the contacts were placed exactly as they were on the test chip. The contacts that were taken for calibration did not have any other test structures within a radius of 30 - 40 μm in their vicinity. This is a sufficient distance between neighboring contacts to ensure that measurements made on a structure are not influenced by the surrounding test structures.

3.2.2. Z_{11} as a calibration metric

As explained earlier, a simple description of the vertical stratification of the substrate is to be determined. Z_{11}, the open-circuit parameter that represents the impedance from the port (at the surface) to the back-plane, is the only parameter that is used in this calibration procedure. There are two reasons for using Z_{11}. First, a Z_{11} measurement can be done independent of other contacts and second, Z_{11} from Eq. (2.4), contains contributions of R_{11} and R_{12} - both of which affect the degree of signal coupling.

---

[1]It is observed that for a heavily doped substrate, the die-size can be small as long as the test structures are not close to the edges of the substrate.

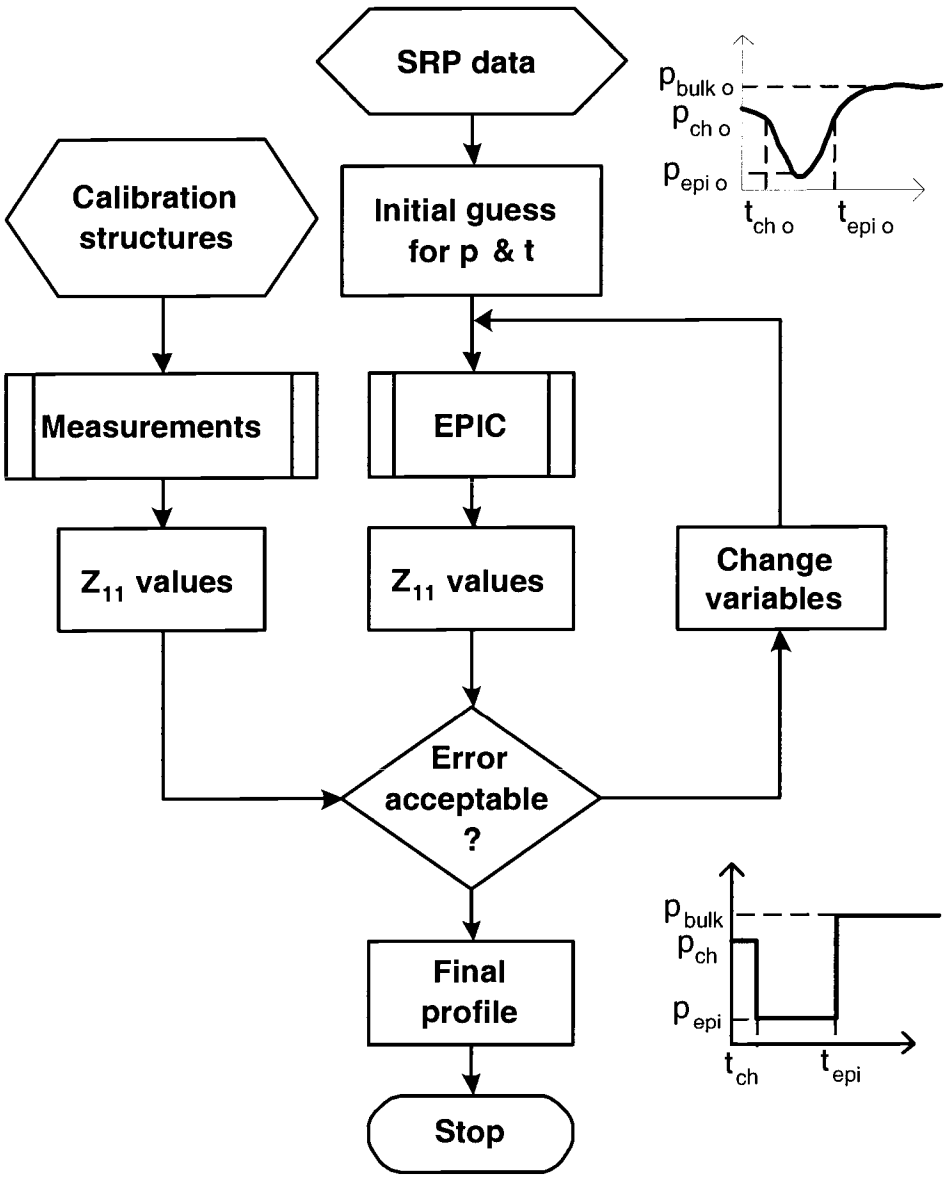

Figure 3.3. Flow-chart for substrate calibration.

3.2.3. Optimization loop

The optimization loop is based on the Levenberg-Marquardt technique [15]. An arbitrary initial guess for the layer resistivities and thicknesses is made based on inspection of the actual SRP data. The variables are the resistivities and thickenesses of the channel stop (ρ_{ch}, t_{ch}) and the epitaxial (ρ_{epi}, t_{epi}) regions.The resistivity of the heavily doped bulk was assumed constant (since the doping level is constant) and taken from the SRP data. The thickness of the fabricated die was $200\mu m$. The thickness of the bulk region is obtained by subtracting the thicknesses of the channel stop and epi layers from the wafer thickness.

The optimization problem that has to be solved is given by:

$$min \quad \frac{1}{2}\sum_{i}\left\{\frac{Z_{11,i\ \ EPIC}(\rho_{ch}, t_{ch}, \rho_{epi}, t_{epi})}{Z_{11,i\ \ measured}} - 1\right\}^2 \tag{3.2}$$

where i refers to the i^{th} test structure used for the calibration.

A simple weighting of the values is inherently achieved by the normalization used in the above objective function. The Z_{11} values from EPIC are divided by the corresponding measured Z_{11} values. This normalization is needed because some of the ports are very small ($0.7\mu m \times 0.7\mu m$) and hence they have much larger Z_{11}'s as compared to other ports ($60\mu m \times 60\mu m$) which have small Z_{11}'s. This can cause the resistivities and thicknesses to be biased and the normalization ensures that all the test cases are weighted equally.

3.2.4. Output of calibration routine

After the calibration routine has completed the optimization, it outputs the final layer resistivities and thicknesses. When EPIC is used with these optimized

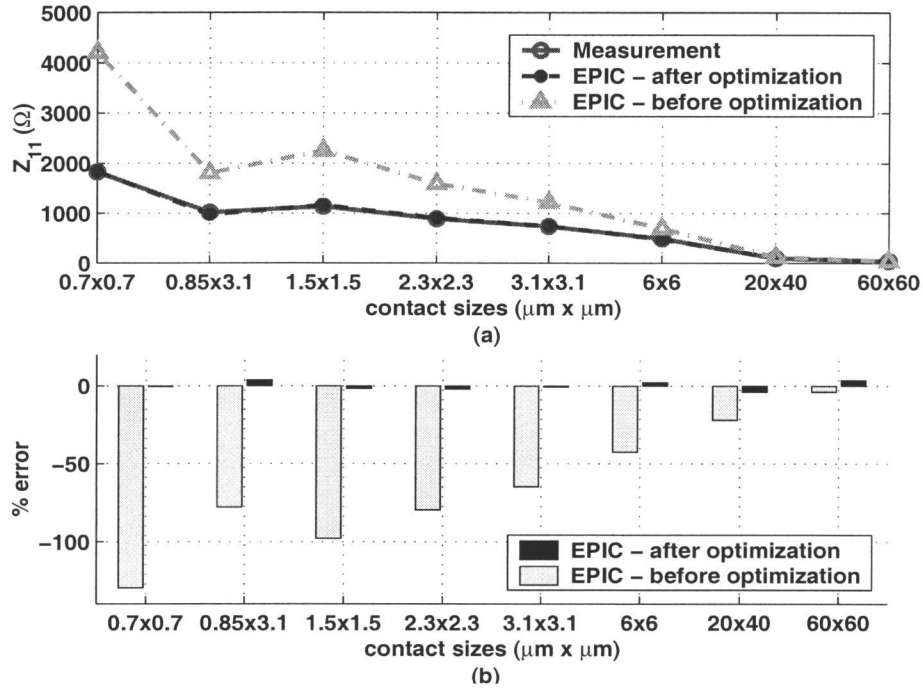

Figure 3.4. Calibration step with Z_{11} for different contact sizes. (a) Values of Z_{11} before and after optimization. (b) Percentage error relative to measurements for the test structures used for calibration.

layer resistivities and thicknesses, the Z_{11}'s for the eight test structures are found to match those used as a reference for the calibration - in this case the measured Z_{11}'s. Figure 3.4 compares the Z_{11} values obtained for the 8 calibration structures before and after the calibration procedure. The contact sizes used are shown in the figure as well. The initial and final Z_{11} values are compared with measurements in Table 3.1. The values of the initial and final resistivities and thicknesses of the channel stop (ρ_{ch}, t_{ch}) and epitaxial regions (ρ_{epi}, t_{epi}) are listed in Table 3.2. As will

be explained in Section 3.4, the final values for the layer resistivities and thicknesses depend on their initial values used for the optimization.

Table 3.1. Z_{11} values from EPIC after optimization are in good agreement with measurements for the structures used in the calibration step.

Contact Size	Z_{11} *(Ω) Measurement*	Z_{11}*(Ω) After Optimization*	*% Relative Error*
$0.7\mu m \times 0.7\mu m$	1830.9341	1837.411	-0.30
$0.85\mu m \times 3.1\mu m$	1016.689	977.430	3.00
$1.5\mu m \times 1.5\mu m$	1138.192	1157.296	-1.67
$2.3\mu m \times 2.3\mu m$	887.186	904.536	-1.96
$3.1\mu m \times 3.1\mu m$	738.027	742.528	-0.60
$6\mu m \times 6\mu m$	488.034	477.487	2.16
$20\mu m \times 40\mu m$	96.961	100.727	3.88
$60\mu m \times 60\mu m$	37.535	36.150	3.70

3.3. Validation of calibration

Chapter 2 explained the measurement methodology for measuring substrate resistances. The previous sections developed the calibration procedure and the motivation for its inclusion in the substrate parasitic extraction flow. This section compares the results from EPIC with those obtained from measurements.

Figure 3.5 compares the pre- and post-optimization Z_{11} values for 7 different structures that were not used in the calibration step. The contact sizes are shown

Table 3.2. Resistivities and thicknesses of layers before and after optimization.

Parameter	*Symbol*	*Initial guess*	*Value After Optimization*
Resistivity of channel stop	ρ_{ch}	$0.6\Omega cm$	$0.205\Omega cm$
Thickness of channel stop	t_{ch}	$1.8\mu m$	$0.9525\mu m$
Resistivity of epi-layer	ρ_{epi}	$6\Omega cm$	$6.587\Omega cm$
Thickness of epi-layer	t_{epi}	$3.2\mu m$	$3.235\mu m$

in the figure as well. As can be seen from the figure, considering all cases, the maximum error after optimization is approximately 10 %. Table 3.3 summarizes the values of Z_{11} for the 7 contacts after optimization which are in close agreement with measurements. This demonstrates that the calibration procedure yields accurate values for Z_{11}.

Figure 3.6 shows the Z_{12} values, for a pair of $0.85\mu m \times 1.5\mu m$ contacts as a function of mutual separation. The Z_{12} values obtained from the calibrated layer thicknesses and resistivities are more accurate than those obtained by using the initial guess. For noise estimation purposes, the values of R_{11} and R_{12} are important and these can be easily calculated from the values of Z_{11} and Z_{12}.

Figures 3.7 and 3.8 show the R_{11} and R_{12} values, respectively, of a pair of $0.85\mu m \times 1.5\mu m$ P^+ contacts as the separation between them is increased from $0.6\mu m$ to $100\mu m$. Using the calibrated layer resistivities and thicknesses, EPIC is able to accurately match measurements. The maximum errors is 7 % in R_{11} and the cross coupling resistance, R_{12}, is predicted accurately to within 10 %.

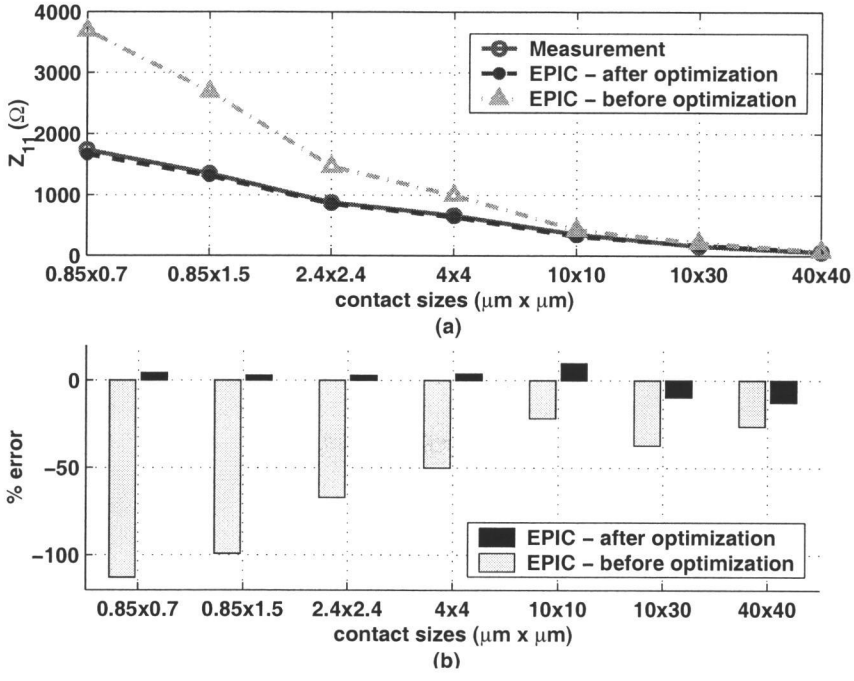

Figure 3.5. Validation step with Z_{11} for different contact sizes: (a) Values of Z_{11} before and after optimization. (b) Percentage error relative to measurements for the test structures used for validation.

Table 3.3. Z_{11} values from EPIC after optimization are in good agreement with measurements.

Contact Size	Z_{11} *(Ω) Measurement*	Z_{11} *(Ω) After Optimization*	*% Relative Error*
$0.85\mu m \times 0.7\mu m$	1734.966	1661.197	4.25
$0.85\mu m \times 1.5\mu m$	1349.478	1312.058	2.77
$2.4\mu m \times 2.4\mu m$	876.386	851.811	2.80
$4\mu m \times 4\mu m$	661.859	636.542	3.83
$10\mu m \times 10\mu m$	350.157	316.073	9.73
$10\mu m \times 30\mu m$	155.321	170.297	-9.64
$40\mu m \times 40\mu m$	58.136	65.407	-12.51

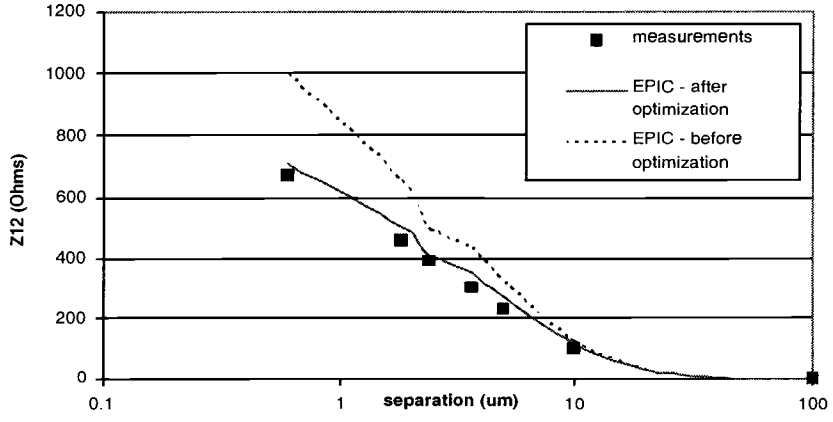

Figure 3.6. Z_{12} values (before and after optimization) of two $0.85\mu m \times 1.5\mu m$ contacts as a function of separation.

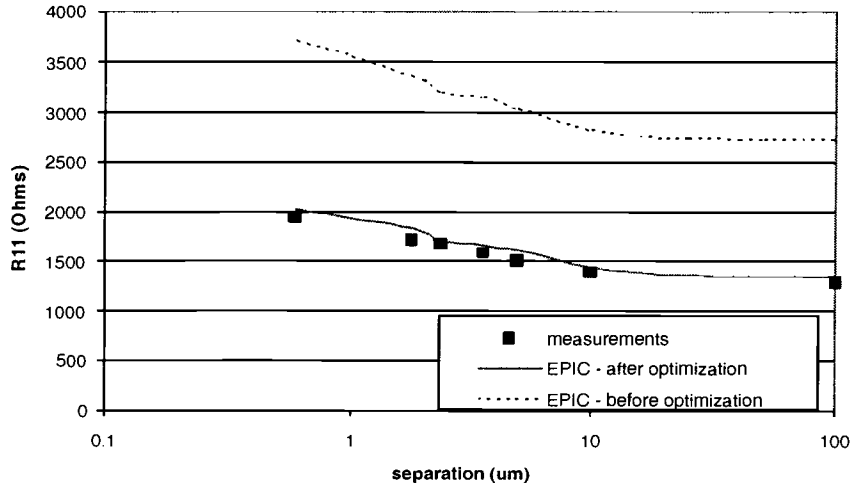

Figure 3.7. R_{11} values (before and after optimization) of two $0.85\mu m \times 1.5\mu m$ contacts as a function of separation.

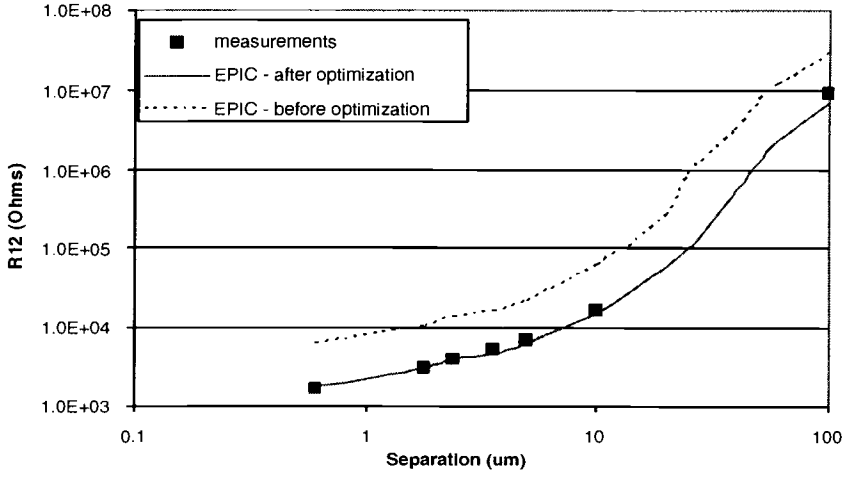

Figure 3.8. R_{12} values (before and after optimization) of two $0.85\mu m \times 1.5\mu m$ contacts as a function of separation.

The above results lead to an accurate prediction of the noise transfer function (NTF) as shown in Figure 3.9. Using the values of R_{11} and R_{12} obtained from EPIC and the initial doping profile (i.e., layer resistivities and thicknesses before optimization), the NTF predicted underestimates the noise by up to 40 %.

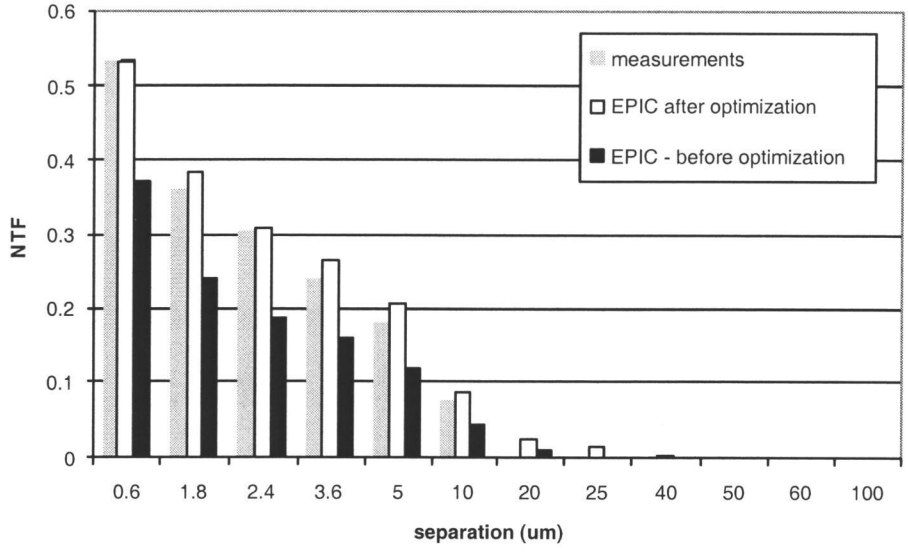

Figure 3.9. Noise transfer function (NTF) is predicted accurately after the calibration procedure for two $0.85\mu m \times 1.5\mu m$ contacts as a function of separation.

Table 3.4 compares the pre- and post-optimization values of the NTF with measured values for the two $0.85\mu m \times 1.5\mu m$ contacts at various separations. As can be seen, as the separation between the ports increases, the value of NTF decreases. A higher value of NTF implies greater coupling as expected. The graph in Figure 3.9 shows a monotonic reduction in the coupling between the ports with increasing separations.

Table 3.4. NTF values from EPIC after optimization are in good agreement with measurements.

Separation (μm)	*NTF Measurement*	*NTF Before Optimization*	*NTF After Optimization*	*% Relative Error*
0.6	0.5324	0.3707	0.5345	-0.4
1.8	0.3584	0.2418	0.3818	-5.5
2.4	0.3041	0.1849	0.3083	-0.4
3.6	0.2353	0.1600	0.2645	-8.3
5	0.1775	0.1185	0.2018	-11.1
10	0.0762	0.0438	0.0851	-11.7
100	0.0001	0.0001	0.0001	0

3.4. Notes of caution

- The calibration module that has been described is not a universal calibration routine. For instance, sometimes it is insufficient to use only the Z_{ii}'s as the calibration parameter. Z_{ii} was an apt calibration metric because the substrate in question was a heavily doped one. The substrate resistances between any two contacts will depend only on their relative location and geometry - provided other contacts are sufficiently far away. Hence the Z_{ii} can be obtained easily for a contact. However, this is not the case in a lightly doped substrate. In a lightly doped substrate, the substrate resistances between any two ports can be affected by other ports on the die. Hence, it is impossible to isolate

the contribution of a single contact, or a pair of contacts. In order to apply this optimization procedure to a lightly doped substrate, it may be necessary to calculate the Thevenin equivalent resistance between the ports of interest using a SPICE simulation. For such a case, SPICE will need to be interfaced with the calibration routine.

- The optimization that has been implemented here is a local optimization routine. The final "optimized" values of the resistivities and thicknesses of the substrate layers depend on the value of the initial guess. It is logical to expect multiple solutions to the layer resistivities and thicknesses because the substrate noise coupling mechanism will depend on the ratio of the resistivities and the ratio of the thicknesses between the layers. Hence, it is quite possible that there can be multiple optimum solutions or local minima.

- The data that has been used for obtaining the macro-model described in Chapter 4 was generated using the substrate profile shown in Figure 3.10. To generate this profile, the initial guess chosen for the resistivities and thicknesses were those output by the Dop2sti program [18] which is part of the SeismIC package from Cadence Design Systems. The values for the resistivities and thicknesses that were output by Dop2sti are also shown in Figure 3.10.

3.5. Summary

This chapter has discussed the motivation behind the use of a calibration procedure and the role it plays in model development and extraction. The various factors that need to be considered before a calibration of the substrate can be

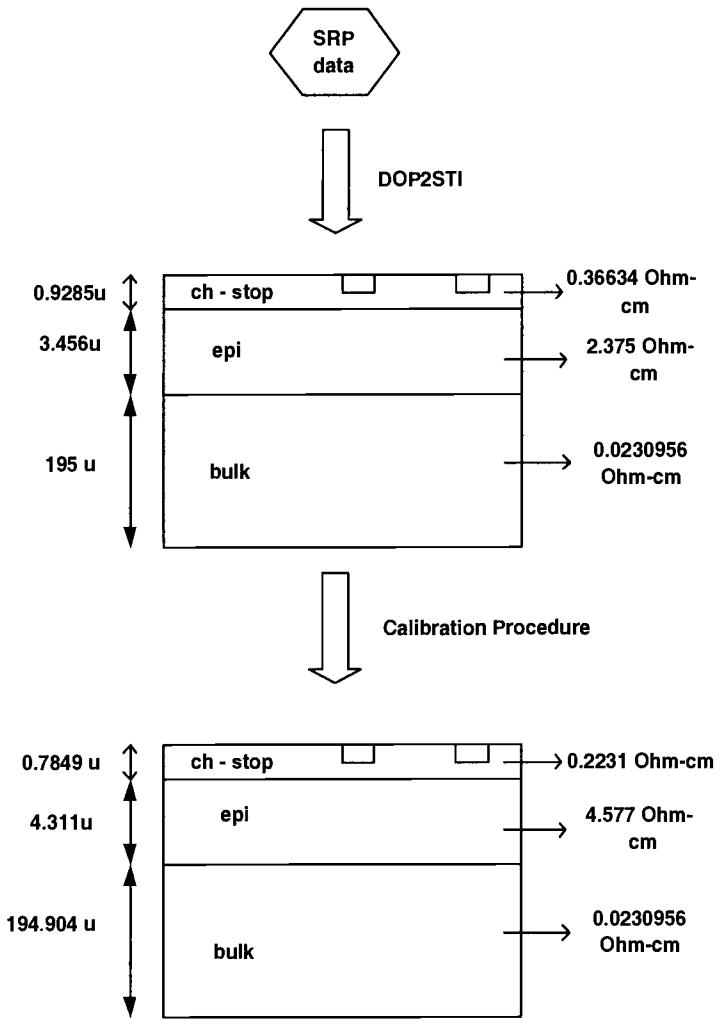

Figure 3.10. The initial guess for the calibration procedure is obtained from the SRP data using the DOP2STI program from Cadence. Also shown is the final profile after the calibration is complete.

undertaken have been verified. The means of integrating the calibration procedure into a standard substrate noise coupling analysis have been explored. The procedure developed and the results presented in this chapter show that it is possible to accurately model a heavily doped epitaxial substrate as a 3 layered structure, with uniform layer resistivities. Furthermore, the Z_{11} of a single contact is sufficient for use in the proposed calibration procedure. Systematic calibration of the substrate is an effective and seamless means of accurate substrate parasitic extraction, thus enabling substrate noise coupling analysis in large mixed-signal SoCs.

4. 3D MACRO-MODEL FOR EPITAXIAL CMOS SUBSTRATES

4.1. Methodology and background

The model formulation to handle multiple contacts requires the use of the two port z-parameters as explained in [21] and [5]. The 3-D macro-model for substrate resistances described in this thesis has been extracted in a similar fashion to the one described in [13]. The basic procedure for the formulation of such a model for N contacts is as follows:

1. The z-parameters for the substrate ports can be obtained either from measurement (as described in Chapter 2) or from 3-D substrate parasitic extraction programs (such as EPIC). The relationship between the substrate resistances and the two port z-parameters are given by Eqs. (2.4) and (2.5).

2. The 2-port z-parameters are calculated for contacts taken two at a time. For N substrate ports, this results in ${}^{N}C_{2}$ 2×2 z-matrices.

3. The ${}^{N}C_{2}$ 2×2 z-matrices are then stamped into a $N \times N$ dense z-matrix as shown in Figure 4.1. This $N \times N$ z-matrix contains contributions of all substrate ports. The matrix is symmetric about its principal diagonal. This is because for a purely resistive representation of the substrate, $Z_{ij} = Z_{ji}$, even if the ports i and j are of different sizes. The diagonal elements of the matrix are the self impedances (Z_{ii}'s) of the ports, representing the impedance from the port (at the surface) to the back-plane.

4. This z-matrix is then inverted to give the conductance matrix, Y.

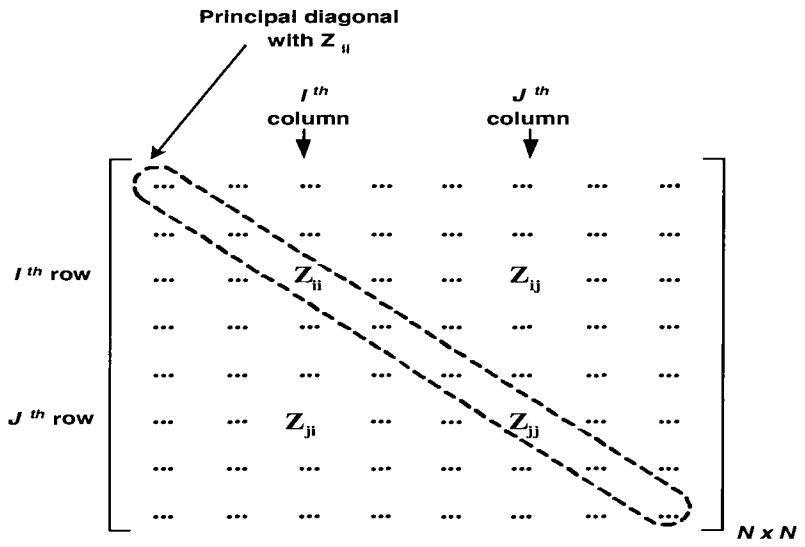

Figure 4.1. The symmetric $N \times N$ Z-matrix.

5. The values in the resistance matrix, R, are obtained as follows:

$$R_{ii} = \frac{1}{\sum_j Y_{ij}} \tag{4.1}$$

$$R_{ij} = \frac{-1}{Y_{ij}} \tag{4.2}$$

As explained in Chapter 2, the Z_{ii} of a port can be measured independent of any other ports. This implies that the expression of Z_{ii} is dependent only on the geometry of the port of interest and the substrate profile.

The concept of a constant Z_{ii} is pivotal to the formulation of the z-parameter based modeling methodology described here. Interestingly, it also is the primary limitation that hinders the extension of such a macro-modeling approach to regions

where effects due to current re-distribution on the ports become significant. This current re-distribution phenomenon occurs due to the proximity of a port to other ports [20].

Consider the case when two substrate ports (assumed here to be of the same size) are moved apart on the surface. R_{12}, the cross resistance between the ports, increases monotonically with separation as is expected (Figure 3.8). It is observed from 3-D simulations and measurements (Figure 3.7) that the value of R_{11} decreases with increasing separation and settles to a constant value beyond a certain distance. Figure 4.2 plots the normalized R_{11} and Z_{11} values for two $2\mu m \times 2\mu m$ contacts as a function of the separation between them. The normalization is done by dividing the Z_{11} (or R_{11}) values at each separation by the corresponding value $Z_{11\,\infty}$ (or $R_{11\,\infty}$), i.e., the value of Z_{11} or R_{11} when the contacts are very far apart (in this case $100\mu m$). As can be seen from Figure 4.2(a), at a separation of about $1\mu m$, the R_{11} values vary by as much as 1.5 times their values at $100\mu m$. However, the corresponding variation of Z_{11} at the same separation is only about 2 % as is evident from Figure 4.2(b). Hence, Z_{11} can be assumed to be a constant for this case.

At this point it is worthwhile to appreciate that the two-port z-parameters model only the behavior of the entire system. They are only a representation that is mapped to the electrical domain in the form of the π-resistive network. Z_{11} contains contributions of all "circuit" elements - R_{11}, R_{12} and R_{22}. The variation in Z_{11} with separation is much less than that observed in R_{11} because R_{11} and R_{12} vary in opposing directions with an increase in separation. Hence, it is reasonable to conclude that these opposing trends cancel each other, resulting in Z_{11} remaining relatively constant.

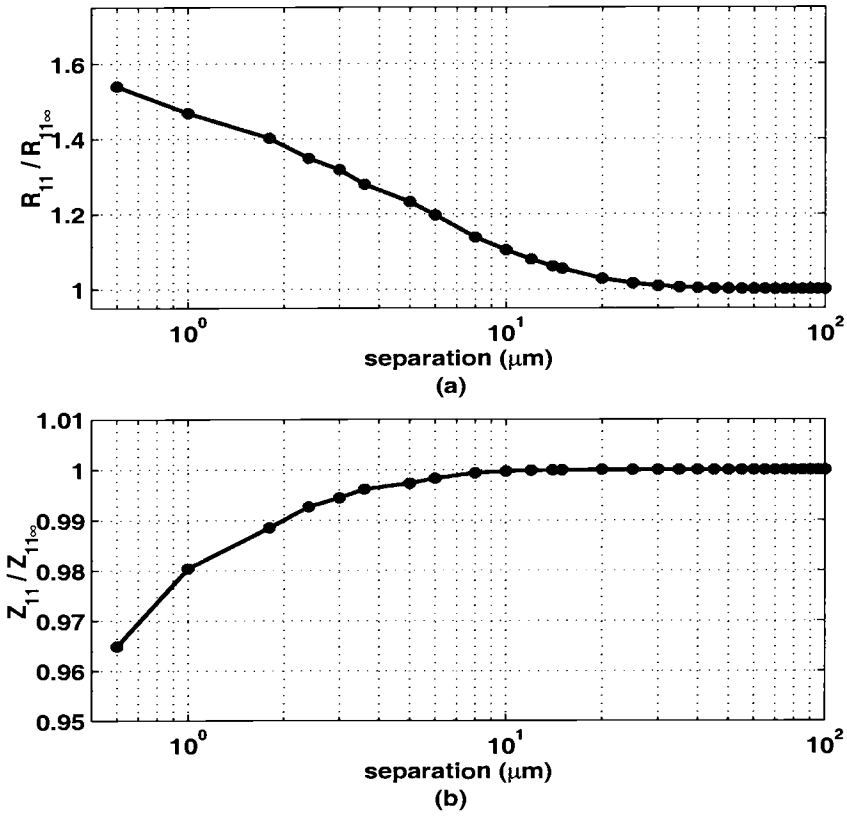

Figure 4.2. The R_{11} and Z_{11} values normalized to their respective values at a very large separation ($100\mu m$) as a function of separation.

In the cases where this "cancelation" is not valid, the Z_{11} varies considerably (almost up to 15 %). This variation in Z_{11} is observed in contact sizes that are about $15\mu m \times 15\mu m$ and larger. The assumption that Z_{11} is constant is then no longer valid. This translates to limits on the separations and contact sizes for which the proposed macro-modeling approach is applicable. This issue is addressed in greater detail in the next chapter.

4.2. Shortcomings of the existing model for multiple contacts and focus of the proposed model

A simple, resistive macro-model for the z-parameters in a heavily doped substrate has been given in [5]. The model is simple and accurate, but it does not address certain key issues. The salient points addressed in the modeling scheme described in this chapter are as follows:

1. It was assumed in [13] that the z-parameter based modeling methodology is not valid for separations below $10\mu m$ because the values of Z_{ii} change. However, as seen from the case of the $2\mu m \times 2\mu m$ contacts in Figure 4.2, the value of Z_{11} varies by only 2 % at a separation of $1\mu m$. Hence, it is reasonable to assume Z_{11} is a constant. This thesis shows that it is possible to extend this z-parameter based macro-modeling approach to separations as small as 1.5 μm.

2. The model for Z_{12} described in [13] is inadequate for separations less than $10\mu m$. This is because at closer separations the behavior of the 2-port system is affected by the lateral current flow in the epitaxial layer [21]. An alter-

nate expression has been developed that models the Z_{12} accurately for these separations.

3. The expression for Z_{12} in the model described in [5] defines the parameter α to be equal to the Z_{11} of the structure obtained when two contacts are merged into one. This "merged contact" is ambiguous and can lead to problems when implementing the model in a CAD frame-work. An example of the possible ambiguity that can arise is shown in Figure 4.3. This problem is not apparent when one considers the coupling between two identical square or rectangular contacts of relatively similar dimensions. However, when the contacts are oriented in different ways or are relatively thin and long, then this problem is highlighted. In the model proposed in this work, the geometric quantities used can be implemented in a CAD framework without any ambiguity. A generic methodology to apply the technique to a large number of contacts has also been addressed.

4. Methods to incorporate this z-parameter based macro-modeling approach into a complete substrate parasitic extraction flow have been addressed. From [5] the limitations of a z-parameter based macro-modeling approach are not apparent. Contact sizes and separations at which the assumptions made for this macro-model are not valid have been determined. Heuristic guidelines about where such a modeling approach can be used have been presented.

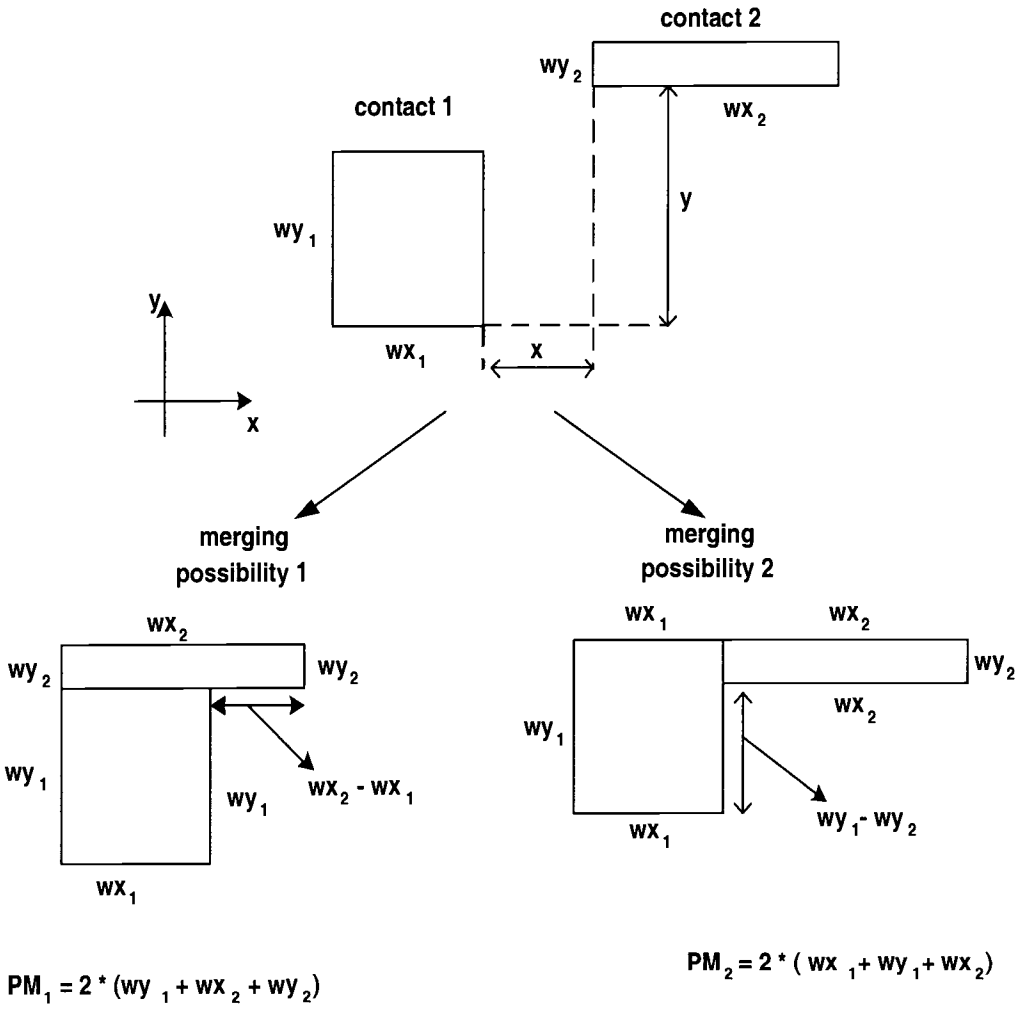

Figure 4.3. There are two possible ways to merge the two contacts. This leads to different values, PM_1 and PM_2, for the "merged" perimeters. This is a problem when the contacts are thin and long, and are of significantly different sizes.

4.3. Enhanced 3-D scalable model for separations less than $10\mu m$

The coordinate axes used for developing the 3-D model are shown in Figure 4.4. EPIC with the calibrated layer resistivities and thicknesses shown in Figure 3.10 has been used to obtain the simulated data points.

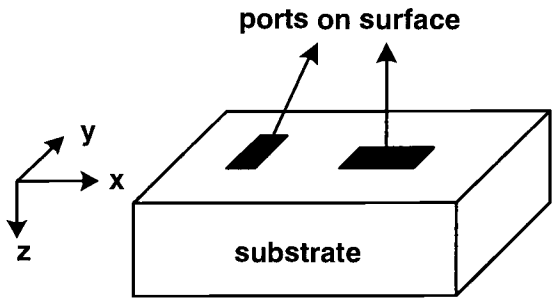

Figure 4.4. Coordinate axes used for determining the macro-model.

A case of three $4\mu m \times 4\mu m$ contacts was analyzed to determine whether the assumption of a constant Z_{ii} is valid. Contact 3 was moved from position A to position C through position B as shown in Figure 4.5. Figures 4.6 (a), (b) and (c) show the variation in Z_{ii} of contacts 1, 2 and 3 respectively.[1] As expected from Figure 4.2, the Z_{ii}'s decrease when the separation between the contacts reaches its minimum, i.e., at position B. At this point, the maximum change in Z_{ii} for each of

[1]Though all three contacts are of the same size, the slight (less than 5 %) difference between their Z_{ii} values is due to the fact that they are not symmetrically placed about the bounding box that EPIC considers as the die boundary.

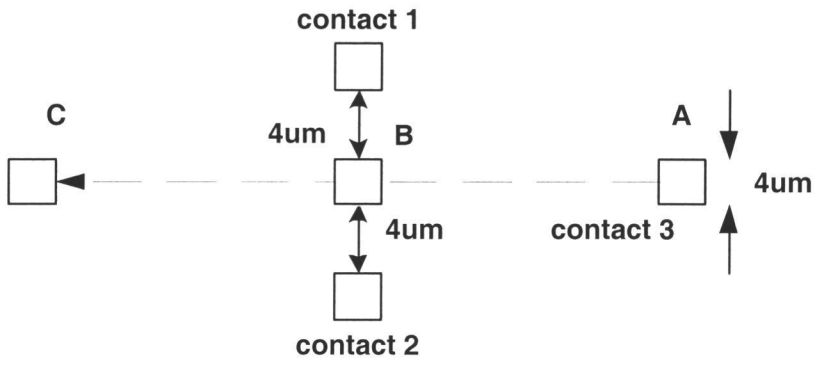

Figure 4.5. Experiment to test the validity of the assumption that Z_{ii} can be considered a constant at small separations.

the contacts is less than 5 % as shown in Figures 4.6 (d), (e) and (f). Hence the assumption of a constant Z_{ii} is reasonable[2].

4.3.1. Expression for Z_{11}

As explained above, the Z_{ii} of a port can be considered reasonably independent of the presence of other nearby ports. Hence, the next step in developing the macro-model is to characterize the effect of contact size on Z_{ii}. Eq. (4.3) is the expression proposed in [5] for Z_{ii}. This expression accurately models the dependence of Z_{ii} on area and perimeter and has been retained.

---

[2]The sharp transitions in the Z_{ii} of contact 3 in Figure 4.6(c) are due to numerical issues with EPIC.

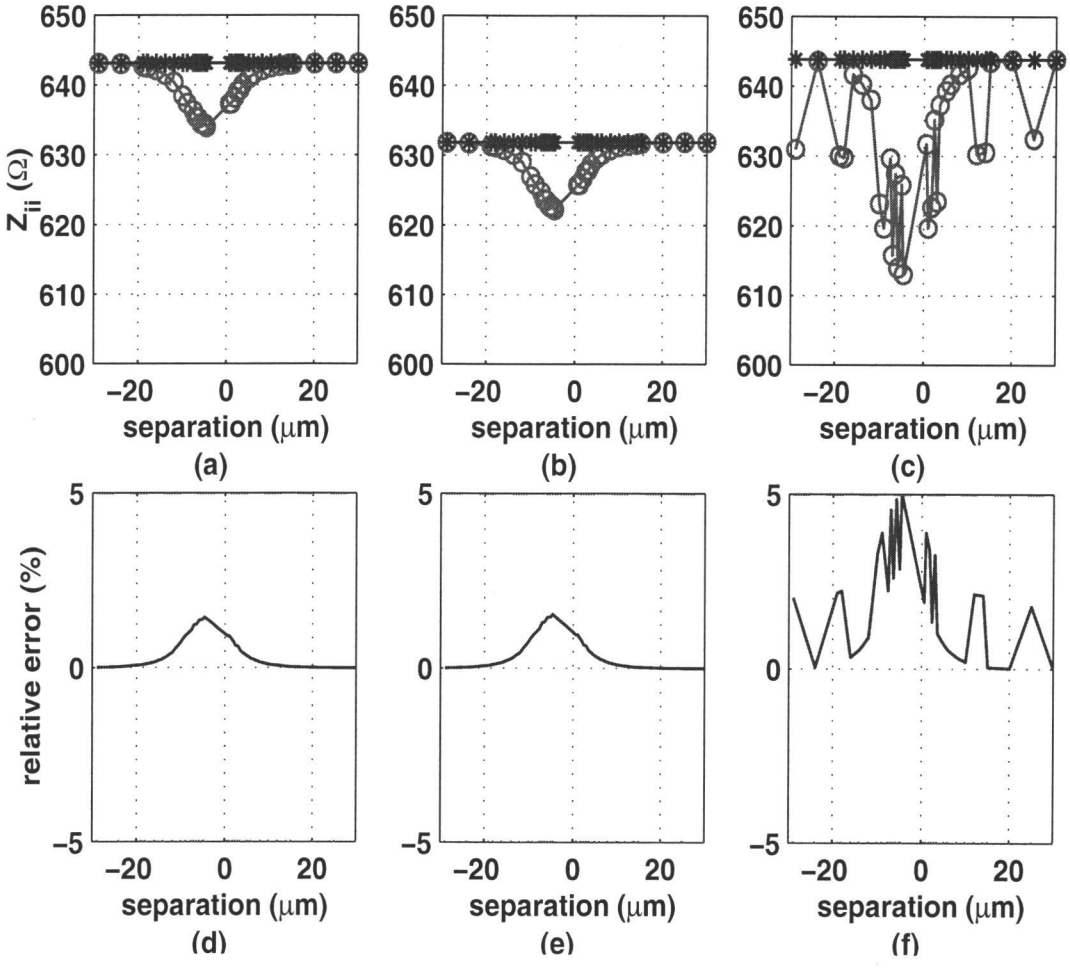

Figure 4.6. Z_{ii} of each contact remains relatively constant for different contact locations.

$$Z_{11} = \frac{1}{K_1 Area + K_2 Perimeter + K_3} \tag{4.3}$$

where K_1, K_2 and K_3 are empirical parameters. Figure 4.7 compares the Z_{ii} values obtained from the model with the data from EPIC simulations. There is good agreement between the model and simulations.

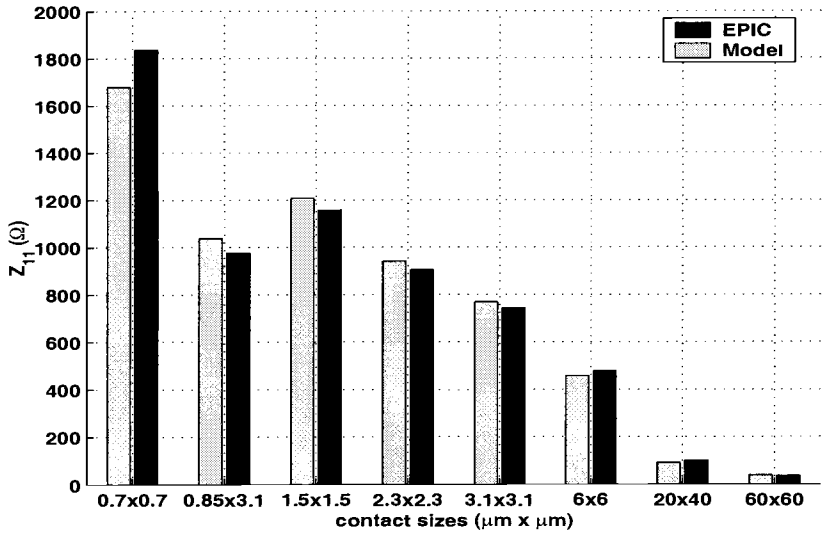

Figure 4.7. The model accurately predicts the Z_{11} for different contact sizes.

4.3.2. Conventions for x and y separations

To model the Z_{12} between two ports/contacts in three dimensions, it is necessary to consider the separation between them, in both the x and y directions. As shown in Figure 4.8(a), x is defined as the separation between the inner edges of the

two contacts. y is defined as the separation in the y-direction between the contact centers.

Since x is the separation between the inner edges of the contacts, it must be greater than or equal to zero. y, however, can be both positive and negative, as contact 2 can be above or below contact 1 in Figure 4.8(a).

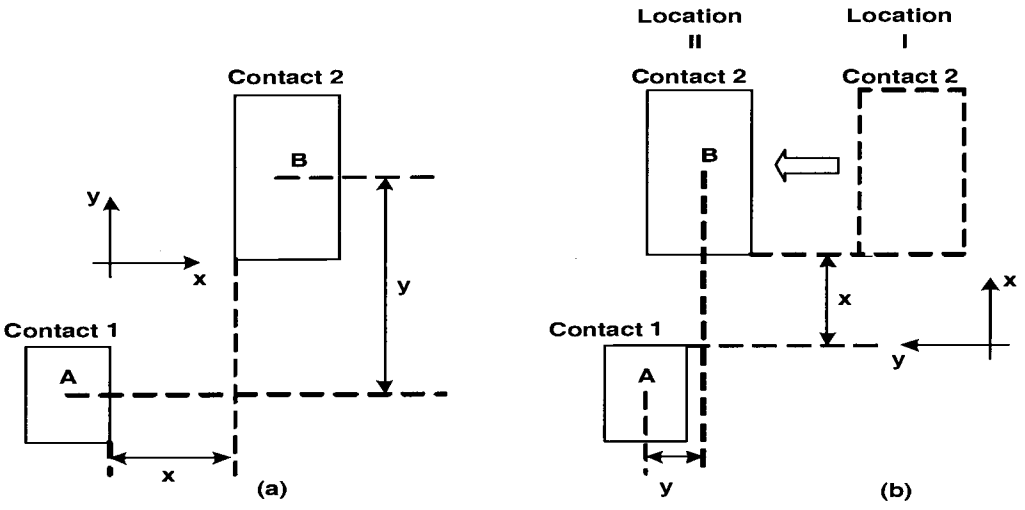

Figure 4.8. x and y separations. (a) Both x and y are positive. (b) When x is zero or negative, the coordinate axes are rotated by 90°.

Next consider the case in Figure 4.8(b) where contact 2 moves from location I to location II. At location II, the x separation as calculated using the coordinate axes shown in Figure 4.8(a) is negative. It then becomes necessary to rotate the coordinate axes by 90° as shown in Figure 4.8(b). The x and y separations are again defined as the distance between the inner edges and between the centers, respectively. This rotation of the coordinate axes by 90° must be done whenever the x-separation is zero or negative. This leads to the important conclusion that

the x and y separations can be used interchangeably - as long it is ensured that one is an edge-to-edge separation, while the other is a center-to-center separation.

x has been defined to be an edge-to-edge separation because as the contacts move closer to each other, there is a significant effect on the values of the two-port z-parameters. This effect on the circuit parameters is due to current distribution and proximity effects between the two contacts. Later, in Chapter 5, a methodology that involves the division of larger contacts into panels is investigated. This requires the problem of calculation of Z_{12} between adjacent panels to be addressed. Here, considering x to be the edge-to-edge separation simplifies model development, because panels that are adjacent are identified by having a zero x-separation.

y has been defined to be a center-to-center separation. As has been explained earlier, the Z_{12} between contacts is maximum when the centers are aligned. A center-to-center definition is useful in modeling as it has an implicit dependency on the sizes of the contacts embedded into it.

4.3.3. Z_{12} model for separation in x-direction

The variation of Z_{12} for two identical contacts is studied as the separation (edge-to-edge) between them is increased[3]. The separation between the inner edges of the contacts (x) is a useful indicator of how close the contacts actually are. If the edges are closer than a certain separation, then as described earlier, proximity effects become important.

---

[3]In this case, Z_{12} does not tend to 0 as $x \longrightarrow \infty$ as this expression aims to model the behavior of Z_{12} with increasing x, only up to a range of about $10 - 12\mu m$.

The variation of Z_{12} with separation for different contact sizes is shown in Figure 4.9. As can be seen Eq. (4.4) models the variation of Z_{12} with x accurately:

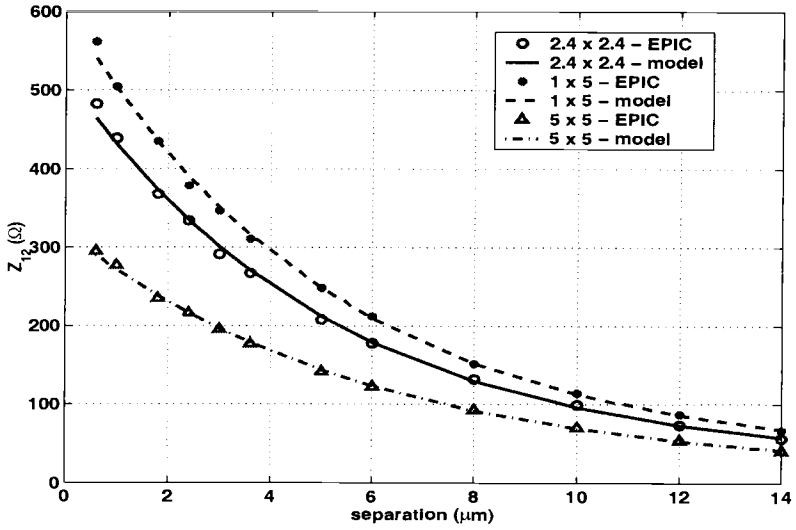

Figure 4.9. Simulations and model for the variation of Z_{12} as function of increasing separation in the x-direction show good agreement.

$$Z_{12}(x) = m_1(e^{-m_2 x} + e^{-m_3 w y_{avg}}) \tag{4.4}$$

where m_1, m_2 and m_3 are parameters that depend on the process and contact dimensions, and wy_{avg} is the average of the contact lengths in the y-direction, as given by:

$$wy_{avg} = \frac{wy_1 + wy_2}{2} \tag{4.5}$$

Next, the dependence of m_1, m_2 and m_3 on the contact dimensions have to be determined. From simulations performed by varying the areas and perimeters of the contacts, the following expressions for m_1, m_2 and m_3 have been determined.

$$m_1 = \frac{A_1}{1 + B_1 P_{avg} + C_1 A_{avg}} \tag{4.6}$$

$$m_2 = A_2 + B_2 P_{avg} + C_2 A_{avg} \tag{4.7}$$

$$m_3 = A_3 + B_3 \left(\frac{P}{A}\right)_{avg} + \frac{1}{C_3 P_{avg}} \tag{4.8}$$

where P_{avg}, A_{avg} and $(\frac{P}{A})_{avg}$ are the average perimeter, area and ratio of perimeter to area of the two contacts, respectively, as given by the equations below.

$$P_{avg} = \frac{Perimeter_1 + Perimeter_2}{2} \tag{4.9}$$

$$A_{avg} = \frac{Area_1 + Area_2}{2} \tag{4.10}$$

$$\left(\frac{P}{A}\right)_{avg} = \frac{\frac{Perimeter_1}{Area_1} + \frac{Perimeter_2}{Area_2}}{2} \tag{4.11}$$

Figures 4.10(a), (b) and (c) show that the expressions (4.6), (4.7) and (4.8) model m_1, m_2 and m_3 accurately for a range of contact sizes.

From Eqs. (4.4) through (4.8) it can be concluded that the macro-model is scalable with contact size and separation, because once the data points and test structures for a particular process have been determined, the constants can be obtained though curve-fitting of this data.

4.3.4. Z_{12} model for separation in y-direction

When dissimilar contacts are placed at different locations relative to each other on the x-y plane, [13] showed that the maximum coupling, for a given x-separation, occurs when the centers of the two contacts are aligned. At this point,

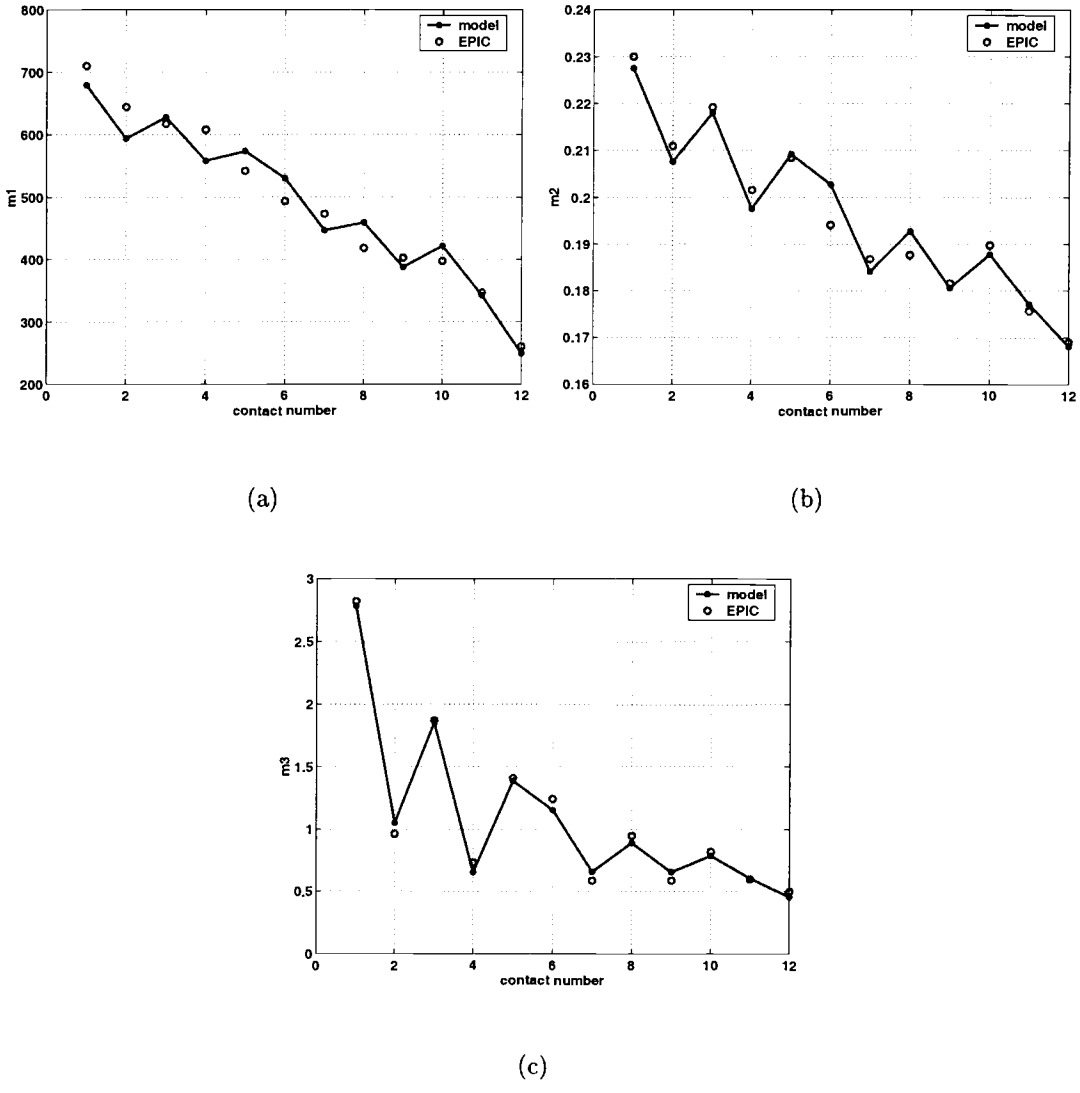

Figure 4.10. m_1, m_2 and m_3 for different contact sizes. The contact sizes corresponding to the contact numbers have been listed in Appendix C.

for the given x-separation, the Z_{12} value is maximum. Further, the Z_{12} values monotonically decrease in a symmetric manner about this point. Also, when two identical contacts are moved in the x-y plane, the coupling (for a given x) is symmetric about the point where the centers are aligned. Hence, this point is chosen as the point of zero y-separation. This is shown in Figure 4.11, where the Z_{12} will be equal at $y = y_1$ and $y = -y_1$ and will be a maximum at $y = 0$. Before developing a model

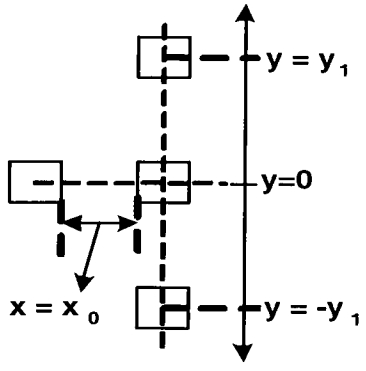

Figure 4.11. Definition of y-separation. $y = 0$ is defined as the point where the centers of the two contacts are aligned.

for the dependence of Z_{12} on y-separation, it is necessary to isolate the dependency of Z_{12} on y-separation. The separation between the contacts is increased in the y-direction, while maintaining the same x separation ($= x_o$) for all contact sizes. The values of Z_{12} are then normalized with respect to the value at $y = 0$. This can be represented as below, where $Z_{12}^N(y)$ is the normalized Z_{12}:

$$Z_{12}^N(y) = \frac{Z_{12}(x_o, y)}{Z_{12}(x_o)} \qquad \forall \quad \text{contact sizes} \tag{4.12}$$

The normalization results in the curves shown in Figure 4.12. As expected, the

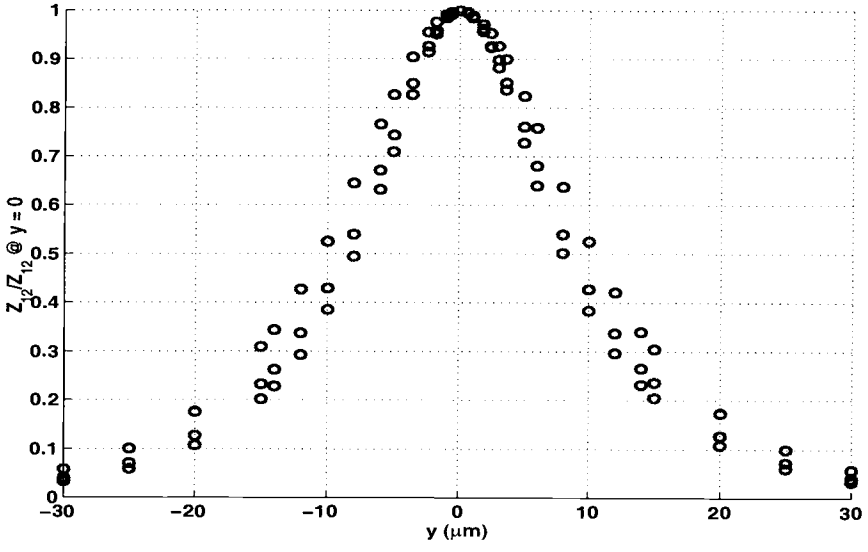

Figure 4.12. The values of Z_{12} as a function of the y-separation, normalized with respect to the value of Z_{12} at $y = 0$.

curves are symmetric about $y = 0$, where the maximum equals 1. This behavior can be modeled as:

$$Z_{12}^N(y) = \frac{1 + m_4|y|}{1 + m_5 y^2} \tag{4.13}$$

where m_4 and m_5 are parameters that depend on contact dimensions. This expression models the behavior of Z_{12} with y-separation correctly, because when $y = 0$, $Z_{12}^N = 1$.

As in the case of x-separation only, expressions for m_4 and m_5 are obtained by analyzing their trends for various contact sizes. This results in the following expressions.

$$m_4 = A_4(1 + B_4 P_{avg}) \tag{4.14}$$

$$m_5 = A_5 + B_5 \log \frac{1}{P_{sum}} + \frac{C_5}{wd_{avg}} \tag{4.15}$$

where wd_{avg} is the average of the diagonals of the contacts as shown in Figure 4.13 and P_{sum} is the sum of the perimeters of the two contacts.

Figures 4.14(a) and (b) show that Eqs. (4.14) and (4.15) model m_4 and m_5 accurately for a range of contact sizes.

Correspondingly, to obtain the actual Z_{12} values, a de-normalization must be done. Eqs. (4.13) through (4.15) predict the behavior of Z_{12} with y for different contact sizes accurately, as is evident from Figure 4.15.

The next step is to integrate the two equations to obtain a model for the dependence of Z_{12} between two contacts based on their size and relative location in the x-y plane.

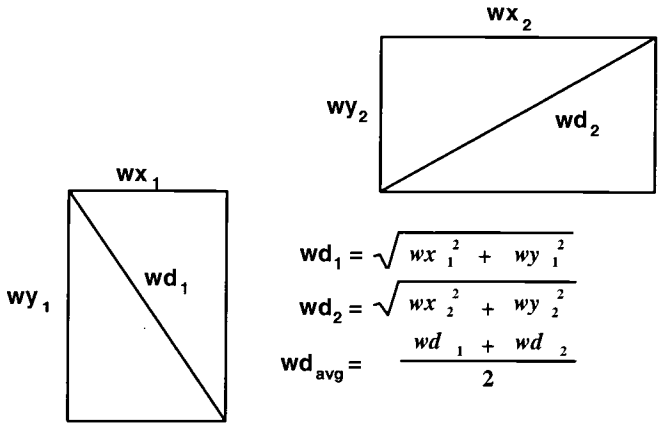

Figure 4.13. Calculation of wd_{avg}.

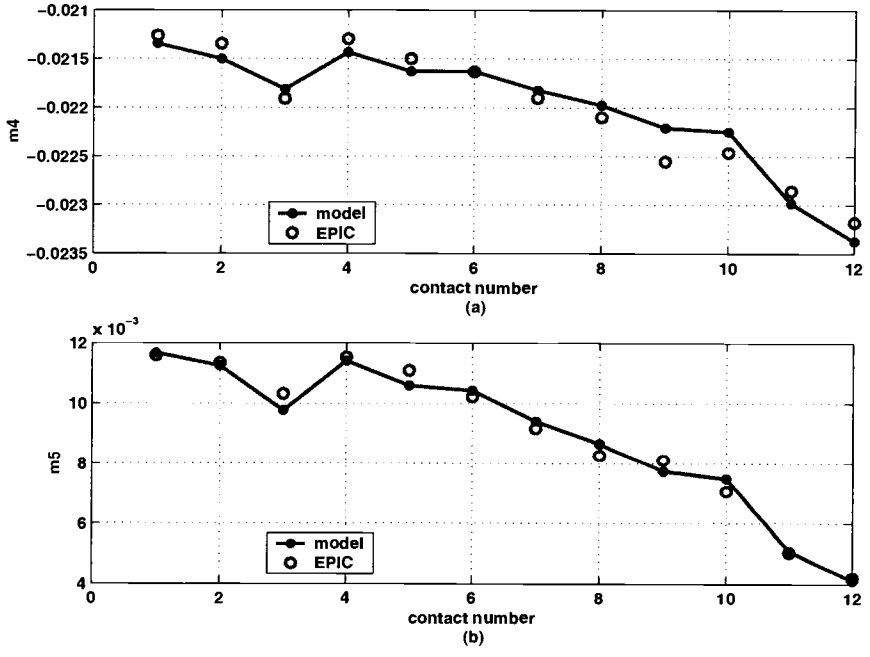

Figure 4.14. m4 and m5 are modeled accurately for a range of contact sizes. The contact sizes corresponding to the contact numbers have been listed in Appendix C.

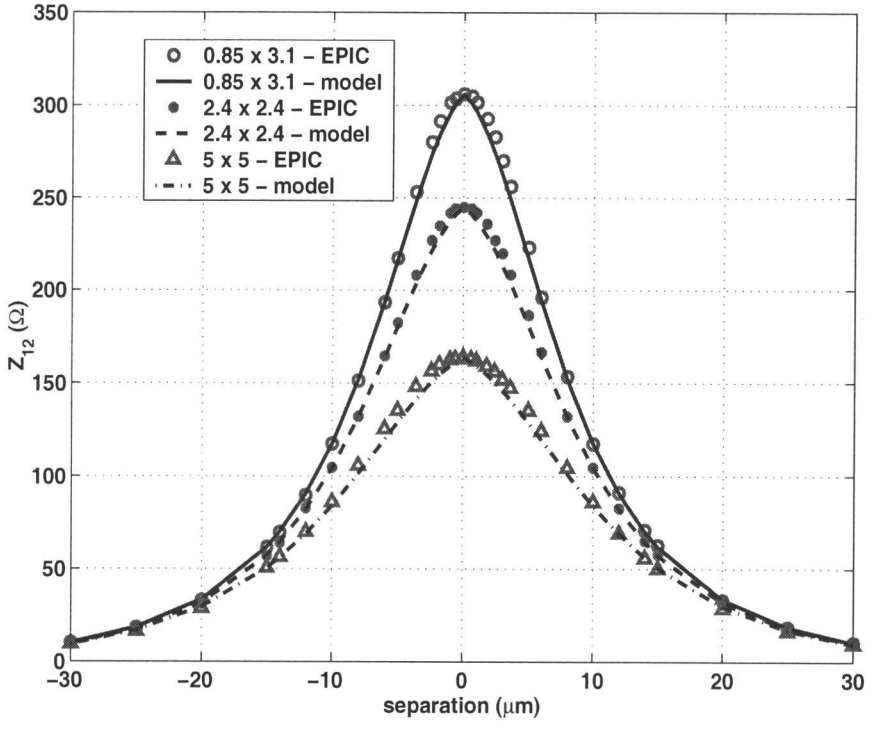

Figure 4.15. The model is in good agreement with simulations for three different contacts that are moved apart in the y direction. The x-separation is $4\mu m$ in all cases.

4.3.5. 3-D model for Z_{12} in the x-y plane

The complete expression that models the behavior of Z_{12} with separations in the x and y directions can be obtained by multiplying Eqs. (4.4) and (4.13). Thus the complete model for Z_{12} based on separation and geometry is given by:

$$Z_{12}(x,y) = m_1(e^{-m_2 x} + e^{-m_3 w y_{avg}}) \left(\frac{1+m_4|y|}{1+m_5 y^2}\right) \tag{4.16}$$

where the expressions for m_1 through m_5 have been presented earlier.

The model that has been developed in this chapter is able to accurately predict the values of the substrate resistances as will be validated in Chapter 5. This model also predicts the noise transfer function for multiple contacts of different sizes that are within a separation of $10\mu m$. The results for all these are presented in Chapter 5.

The model development procedure is summarized in Figure 4.16. A function has been implemented in MATLAB, using the same nonlinear optimization technique that has been used in the calibration procedure described in Chapter 3.

4.4. CASPER

The calibration routine procedure in Chapter 3 and the curve-fitting approach described in the previous section can be combined to give a unified methodology for developing scalable macro-models of the substrate. The overall flowchart for a Comprehensive and Automated Substrate Parasitic Extraction Routine (CASPER) is shown in Figure 4.17. SRP data from the foundry and a set of reference values for the calibration metric (Z_{11} in this case) are used to calibrate a

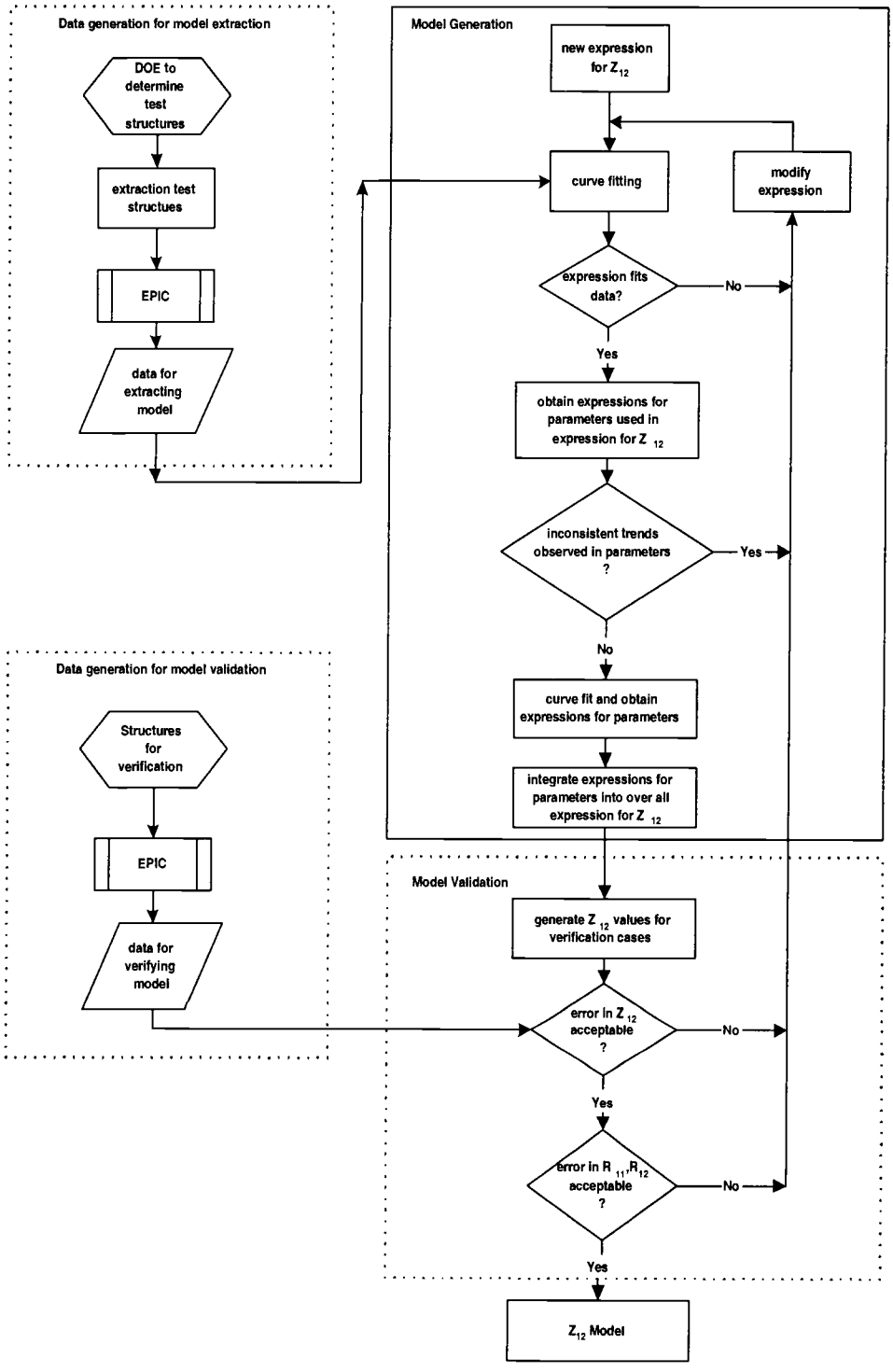

Figure 4.16. The generic flow of a curve fitting methodology to extract the macro-models for Z_{12} for accurate substrate resistance prediction.

3-D Green's function based substrate parasitic extractor. A design of experiments (DOE) analysis determines the test structures to be used for model extraction. The 3-D substrate parasitic extractor is used with the calibrated layer resistivities and thicknesses to obtain the data points (here z-parameters) for the test cases. These data points are used by the curve-fitting engine to extract a macro-model for the substrate. The engine uses a non-linear least squares curve-fitting technique to extract the macro-model. The resistance network can be obtained from this z-parameter based macro-model by inverting the z-matrix and can be stored as a SPICE subcircuit for later analysis. On the other hand, the z-parameter representation of the network can be combined with the digital switching noise information [22] to directly yield the vector of noise voltages at the nodes of interest. Also shown in the figure are the various software platforms for which the different sections of CASPER have been implemented. The respective interfaces to a Green's function based extractor, EPIC in this case, for the calibration and curve-fitting engines has been implemented as well.

4.5. Summary

This chapter has provided the background and presented a methodology to extract scalable models for substrate coupling parasitics. Using this methodology, models for the z-parameters for heavily doped substrates have been developed. This automated approach can be extended for different substrates and can lead to a quick development of such empirical models. The next chapter shows that the models proposed here are applicable to a general case of multiple contacts of various sizes. The limitations of the modeling approach are also described.

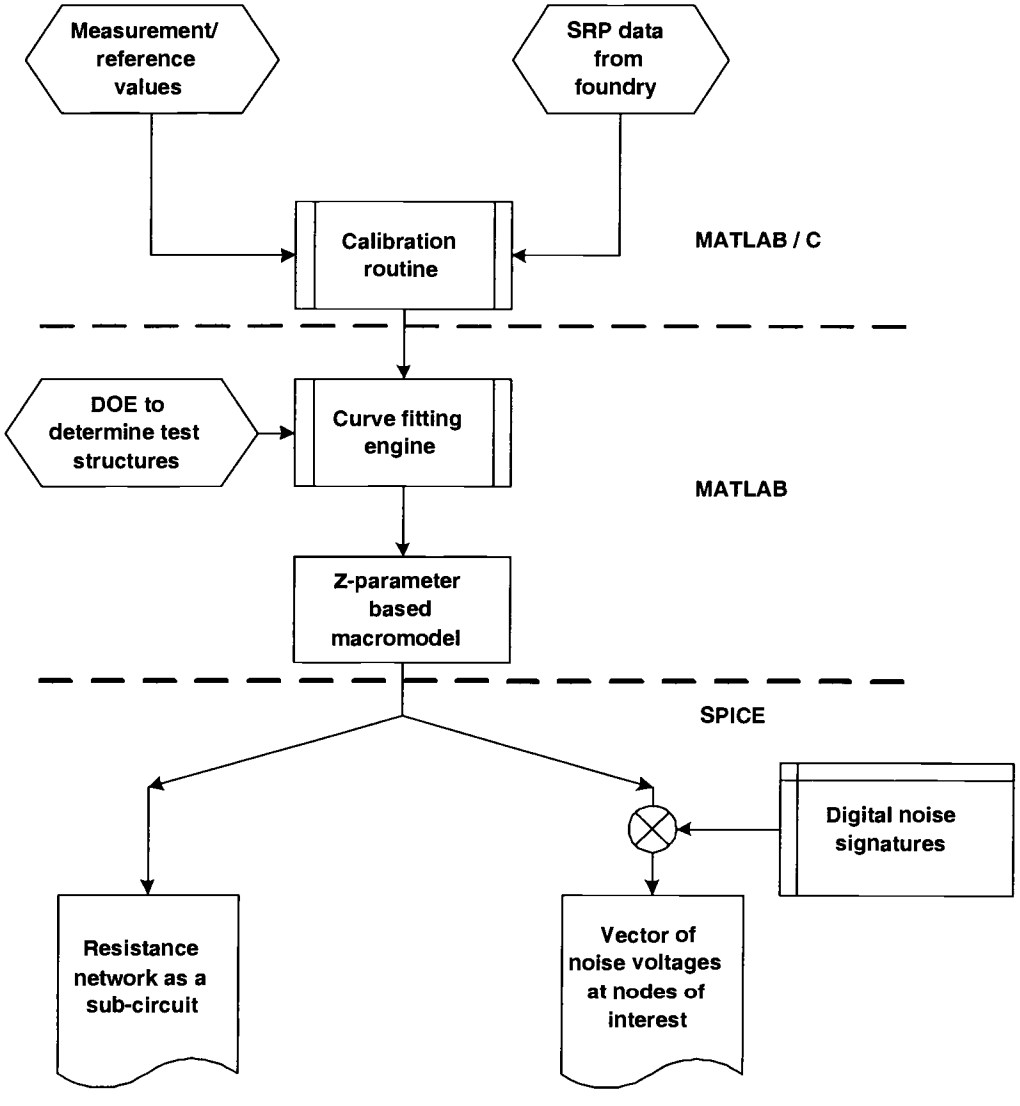

Figure 4.17. The CASPER methodology to extract scalable substrate noise coupling models for silicon substrates.

5. VALIDATION OF 3-D SCALABLE MACRO-MODEL

This chapter presents validation results for the 3-D macro-model proposed and developed in Chapter 4. The model is compared with measurement data and simulation results. The limitations of the z-parameter based macro-modeling approach have also been identified.

5.1. Validation of model for x-separations

The model in Eq. (4.4) for Z_{12} as a function of separation in the x-direction is verified first. The z-matrix obtained using Eqs. (4.3) and (4.4) was inverted and the substrate resistances were calculated using the procedure outlined in Section 4.1. The resistance values are then compared with measurements made on the fabricated test structures described in Chapter 2. Figure 5.1 compares the values of R_{12} obtained using the model and those obtained from measurement of two different contact sizes. As can be seen, the model predicts the values of R_{12} accurately.

5.2. Validation of model for both x and y separations

The complete expression that models the behavior of Z_{12} with x and y separations is given by Eq. (4.16). The model predicts the Z_{12} values between contacts to within 15 % of EPIC simulations as seen in Figure 5.3. The contacts are approximately within $10\mu m$ of each other - and are separated in both the x and the y directions as shown in Figure 5.2.

As explained in Chapter 3, the actual values of the resistances are important from a circuit design perspective. Figures 5.4 and 5.5 show that the resistance values

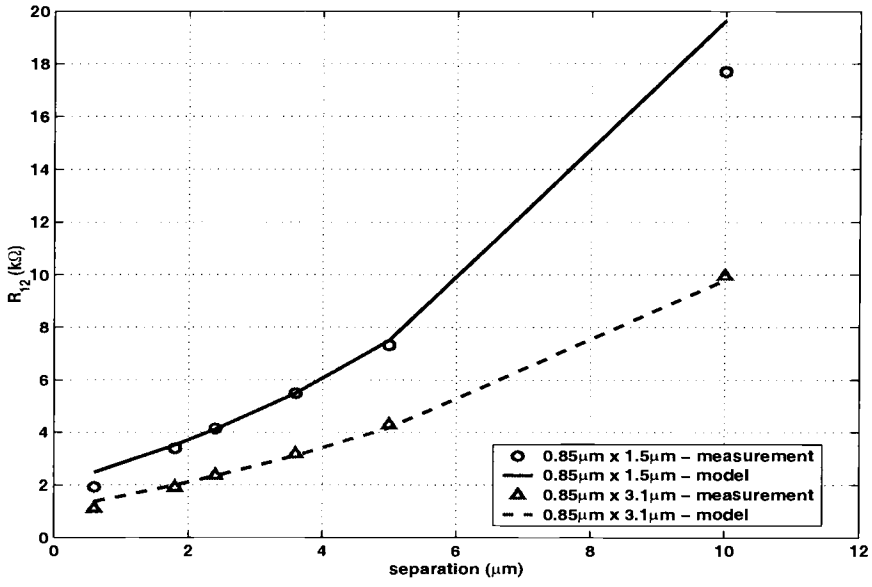

Figure 5.1. The model accurately predicts R_{12} as a function of separation, x.

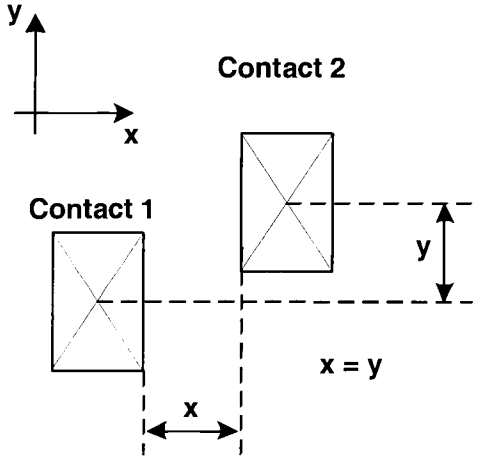

Figure 5.2. Experiment for verification of the Z_{12} model for x and y separations. In this figure $x = y$. The Z_{12} values are plotted in Figure 5.3

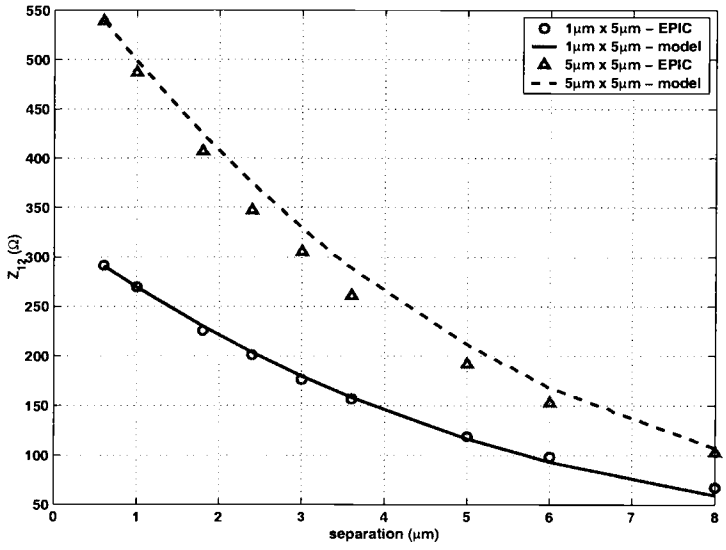

Figure 5.3. The model accurately predicts Z_{12} with separation in the x and y directions. The separation in the x-direction is equal to that in the y-direction for this figure.

obtained from the above z-parameter models are in good agreement with those from EPIC.

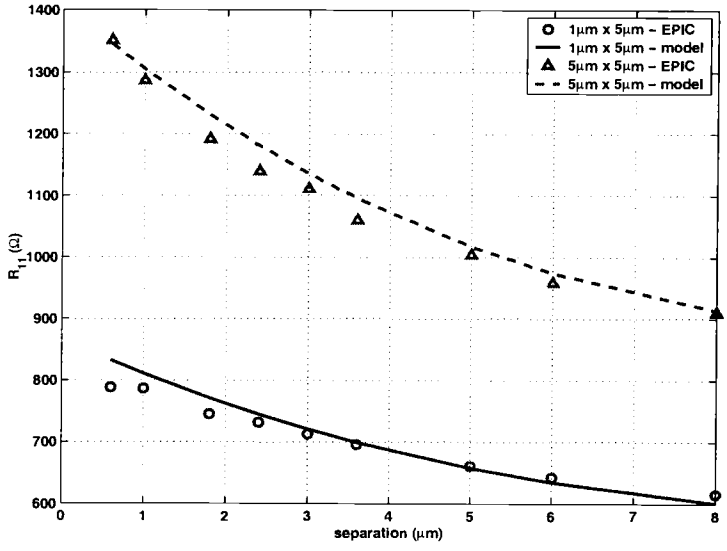

Figure 5.4. The model accurately predicts R_{11} with separation in the x and y directions. The separation in the x-direction is equal to that in the y-direction for this figure.

The noise transfer function (NTF) introduced in Chapter 2 is the quantity of interest for circuit designers. The NTF depends on the values of both R_{11} and R_{12} and is predicted accurately as shown in Figure 5.6.

5.3. Validation of model for a 3 contact example.

The z-parameter based macro-model is verified for multiple contacts in this section. The three contact case of Figure 5.7 was simulated with EPIC and the methodology outlined in Section 4.1 was applied to obtain the resistances between

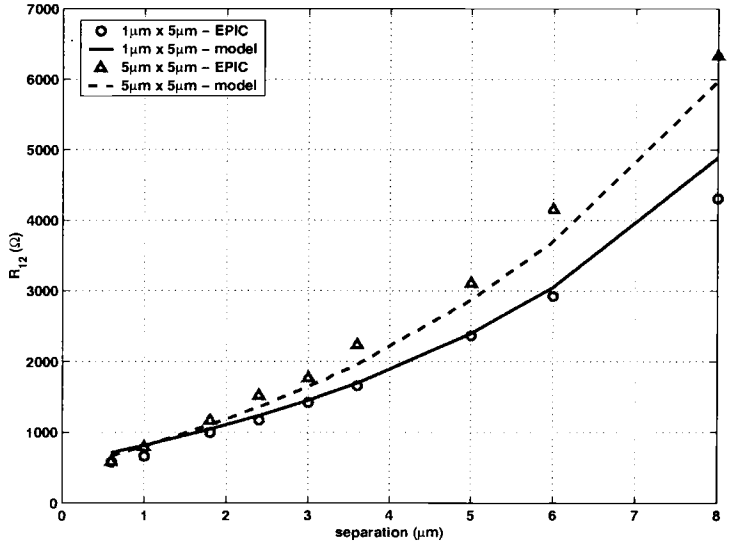

Figure 5.5. The model accurately predicts R_{12} with separation in the x and y directions. The separation in the x-direction is equal to that in the y-direction for this figure.

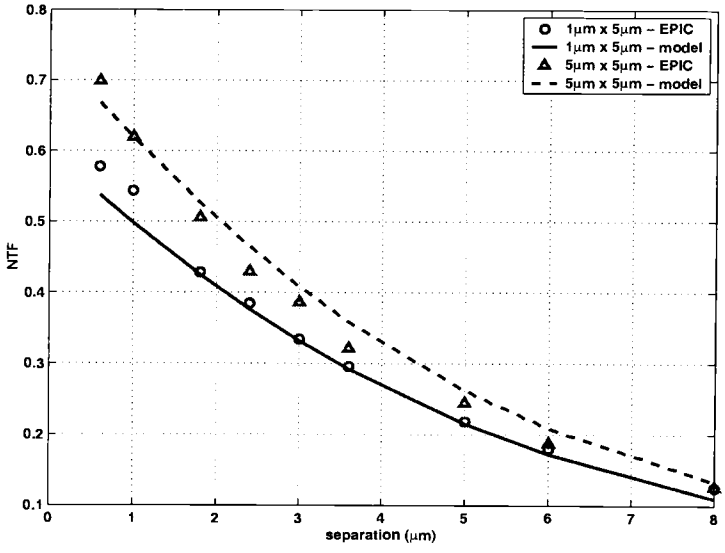

Figure 5.6. The model accurately predicts the NTF with separation in the x and y directions. The separation in the x-direction is equal to that in the y-direction for this figure.

the ports. Table 5.1 compares the resistance values from EPIC with those obtained using the model for this example. The resistance values are within 20 % of simulations.

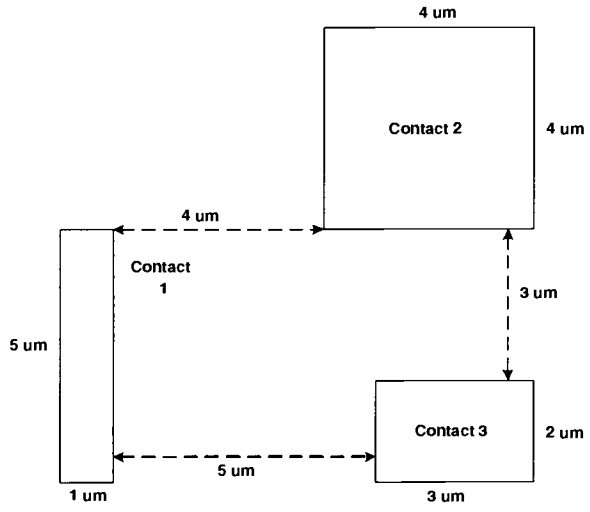

Figure 5.7. The three contact case that was simulated to verify the application of the model to multiple contacts.

5.4. Extension of 3-D macro-model to separations greater than $10\mu m$

The model described thus far was developed specifically to model the behavior of the z-parameters as a function of separations which are less than $10\mu m$. However, the same expression can be used to model the z-parameters for separations greater than $10\mu m$. The data that needs to be supplied for the curve-fitting must be the z-parameter values for separations greater than $10\mu m$. This means the

Table 5.1. Resistance values from the model are in close agreement with those obtained from EPIC for the three contact case of Figure 5.7.

Resistance	*EPIC* (Ω)	*Model* (Ω)	*Percentage error %*
R_{11}	1175.82	1231.95	4.8
R_{22}	9340.98	953.46	2.1
R_{33}	1475.41	1705.66	15.6
R_{12}	3303.79	3069.74	7.1
R_{13}	4436.12	3887.01	12.4
R_{23}	1949.89	2123.02	8.9

same functional forms proposed in Chapter 4, can be retained for Z_{12} and for the parameters m_1 through m_5 for separations greater than $10\mu m$.

Figures 5.8 and 5.9 show the Z_{12} and R_{12} values, respectively, as a function of separation in the x-direction for two differently sized contacts. As can be seen, the model captures the behavior of Z_{12} and R_{12} accurately beyond a separation of $10\mu m$.

In [5], the expression for Z_{12} for separations greater than $10\mu m$ was given by:

$$Z_{12} = \alpha e^{-\beta x} \tag{5.1}$$

where β is a process dependent parameter. α is defined to be the Z_{11} of the contact obtained by merging the two contacts between which Z_{12} was being determined. A discussion on the possible ambiguity that can arise from this concept of merging of contacts has been presented in Section 4.2. This translates to an ambiguity in the

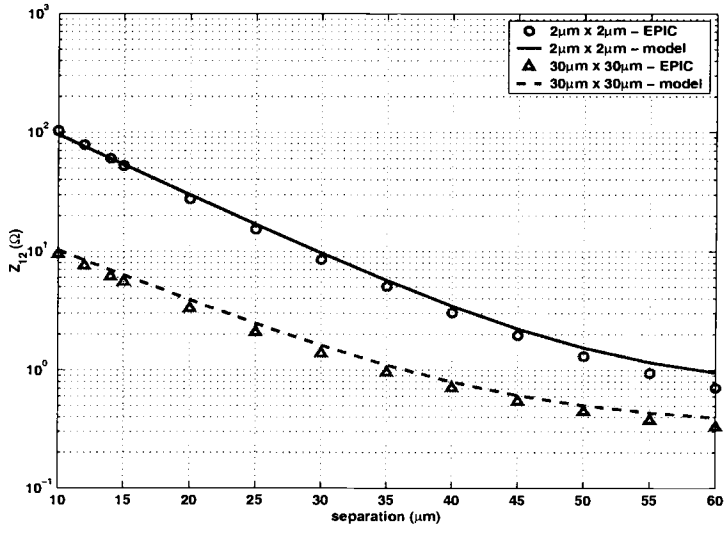

Figure 5.8. The model accurately predicts Z_{12} with separation beyond $10\mu m$ for different contact sizes. A logarithmic (base 10) scale is used for the Y-axis.

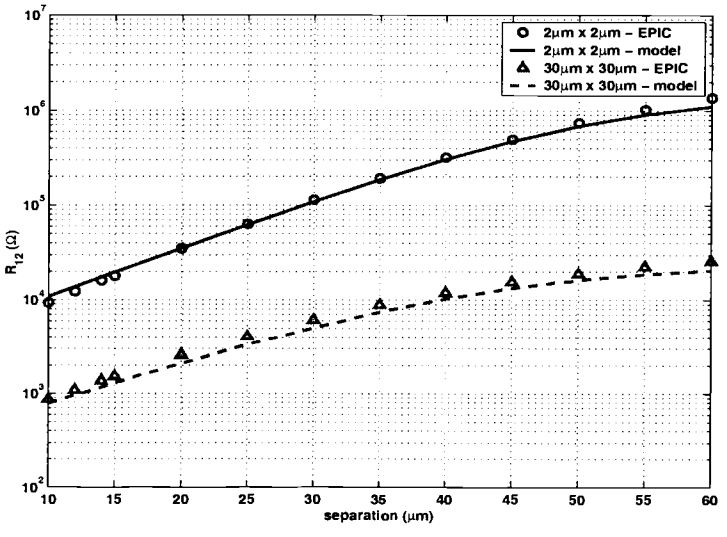

Figure 5.9. The model accurately predicts R_{12} with separation beyond $10\mu m$ for different contact sizes. A logarithmic (base 10) scale is used for the Y-axis.

calculation of α and hence in the final value of Z_{12}. This ambiguity can be solved by using the model proposed in this chapter.

5.5. Limitations of the z-parameter based macro-model

The extraction methodology for the macro-model and its accuracy have been verified with the results presented thus far. The results show that the model is valid over a wide range of separations and contact sizes. A model is incomplete, however, if its limitations are not identified. Assumptions are made during the formulation of any model. When these assumptions are no longer valid, the model will then be inaccurate.

The primary limitation of the macro-model, as mentioned in Chapter 4, is due to the proximity of contacts. The proximity effect is pronounced in the case of large contacts. In Figure 4.2 it was seen that the variation in Z_{11} for a pair of $2\mu m \times 2\mu m$ contacts is minimal. However, from Figure 5.10, it is evident this is not the case as the contact sizes increase. The figure plots the normalized Z_{11} values for contacts as a function of the separation between them. The normalization is done by dividing the Z_{11} values at each separation by the corresponding value ($Z_{11\,\infty}$) when the contacts are very far apart ($100\mu m$). Four different contact sizes have been investigated.

As can be seen from the figure, Z_{11} for all the contacts is relatively constant until the separation becomes less than $10\mu m$. Then the Z_{11}'s vary considerably with decreasing separation. This variation clearly depends on the size of a contact. Hence, to be able to use the z-parameter based modeling approach one must know *a-priori* the separations at which the proximity effect becomes significant. A relation

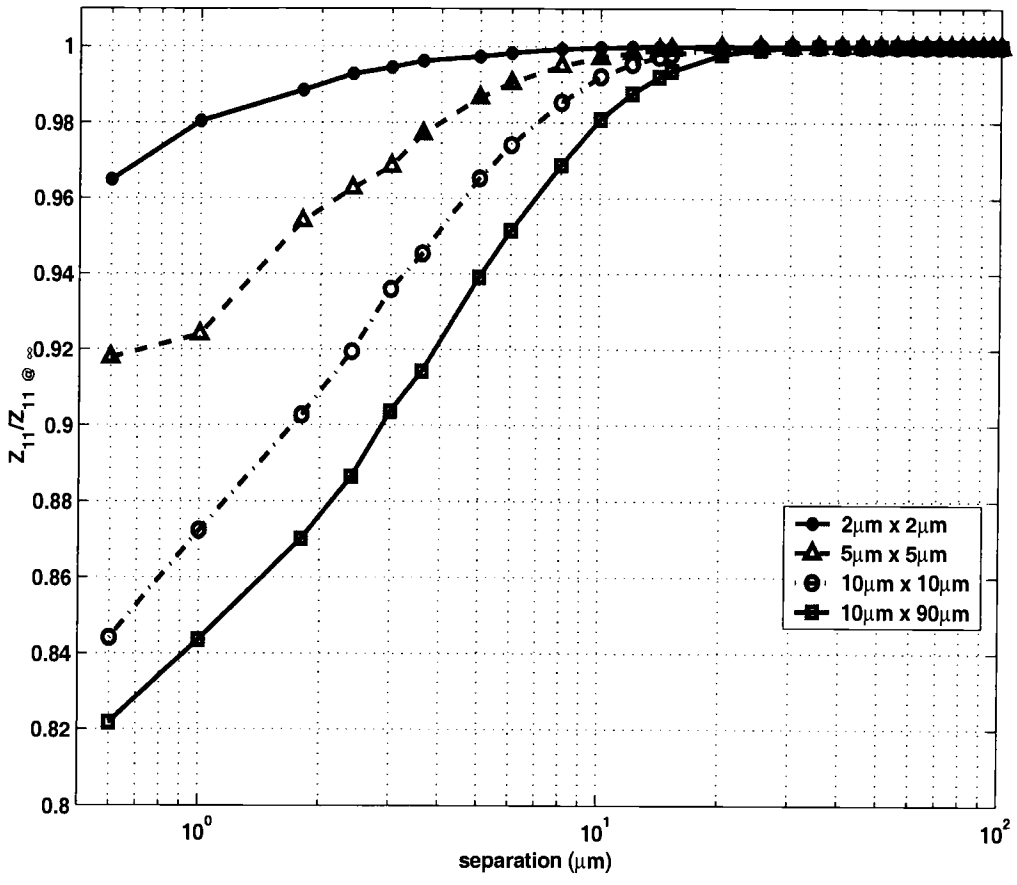

Figure 5.10. The Z_{11} values normalized to their respective values at a very large separation ($100\mu m$) as a function of separation for 4 different contact sizes.

between the absolute size of the contacts and the separation between them needs to be developed.

The z-parameter based approach fails as it now becomes necessary to include a dependency of a neighboring contact on the Z_{ii} value. This contradicts the assumption that the Z_{ii} of a contact is independent of other contacts. Incorporation of a dependency on neighboring contacts on the Z_{ii} implies, for an N-port case, each diagonal element in the $N \times N$ matrix will have a dependence on each of the N other ports. It is, therefore, impossible to build the over-all Z-matrix by stamping the 2×2 two-port Z-matrices as described in Section 4.1.

A reasonable bound must be established for the maximum allowable variance in Z_{11} with respect to its value at ∞. A practical value for this tolerance would be 5 %. This corresponds to a contact size of about $5\mu m \times 5\mu m$ from Figure 5.10.

For contacts sizes larger than the ones permitted by the bounds, an approach based on the discretization of the contacts into panels has been proposed in the following section.

5.6. Division into panels - a possible methodology to extend the z-parameter based approach

The computational efficiency of the z-parameter based macro-modeling approach over traditional approaches that divide the contacts into smaller panels is addressed in [12]. Using the z-parameter based approach, the size of the matrix to be inverted is reduced by orders of magnitude. This is possible primarily due to the scalability of the macro-model with contact dimensions. This implies that the

z-parameter based approach, as compared to other panel-based approaches, can be used for problems with a larger number of contacts.

However, an important assumption in the formulation of the z-parameter based approach was that Z_{ii} is constant. From the results presented in the previous section, it is evident that this assumption is not valid for cases where proximity effects become important. Hence, it is necessary to reformulate the methodology to account for such cases.

A proposed solution is to embed the z-parameter based macro-model in a *traditional* panel-based substrate parasitic extraction. The panels are assumed to be equipotential and the current density across them is uniform. This is similar to the pre-processed boundary element approach described in [21]. However, the main difference is that the proposed solution does not involve dividing the distance between two ports into a set of heuristically determined intervals.

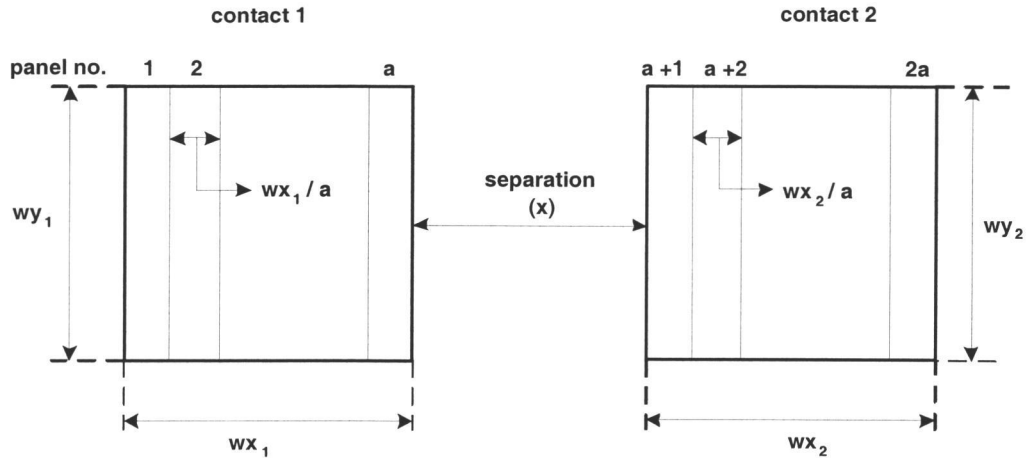

Figure 5.11. Division of two large square contacts into narrow panels to account for the proximity of the two contacts. Both contacts have the same number of panels.

As shown in Figure 5.11, two large contacts are divided into an array of panels. The extraction algorithm used in this procedure is as follows[1].

Phase - I: Initial set-up.

* Divide the *two* contacts into a panels each.

* Calculate the sizes of the panels and separation between them based on geometric data.

Phase - II: Calculation of panel-level Z-matrix (Z_P).

* Z_P is a $2a \times 2a$ matrix.

* Diagonal elements of Z_P are calculated (Eq. (4.3)).

* To calculate non-diagonal elements:

for $i = 1$ to $(2a - 1)$

for $j = (i + 1)$ to $2a$

if panels are adjacent,

$Z_P(i, j) = Z_{ii}$ of "merged" panel (Eq. (4.3))

else

$Z_P(i, j) = Z_{12}$ between the panels (Eq. (4.16))

end

end

---

[1]A MATLAB function was written to verify if this approach can account for proximity effects. The following assumptions have been made for simplicity: (a) only a two-contact case has been investigated, (b) both the contacts are divided into the same number of panels, and (c) only a 1-D discretization into panels has been assumed.

Phase - III: Calculation of two-port Z-matrix for verification.

* Y_P = inverse(Z_P) is the panel level Y-matrix.

* First calculate the resistances R_{11}, R_{12} and R_{22}.

To calculate self-resistances R_{11} and R_{22}:

for each contact

for i = all panels on the current contact

$$R_{ii} = \sum \frac{1}{sum(Y_P(i,:))}$$

end

end

To calculate cross-resistance R_{12}:

for i = panels on contact 1

for j = panels on contact 2

$$R_{ij} = \frac{1}{\sum(Y_P(i,j))}$$

end

end

* Calculate two-port Y matrix (Y_{two}) from the resistances above.

* Calculate two-port Z matrix (Z_{two}) by inverting Y_{two}.

The Z_{11} of the two-port Z-matrix obtained from the above procedure is plotted as a function of separation in Figure 5.12. As can be seen from the figure, the two-port Z-matrix obtained after applying the paneling approach can predict the decrease in Z_{ii} as the separation between the contacts gets smaller. This key behavior is not

exhibited by the two-port Z-matrix obtained by using only the macro-model as is seen from the straight line shown in Figure 5.12.

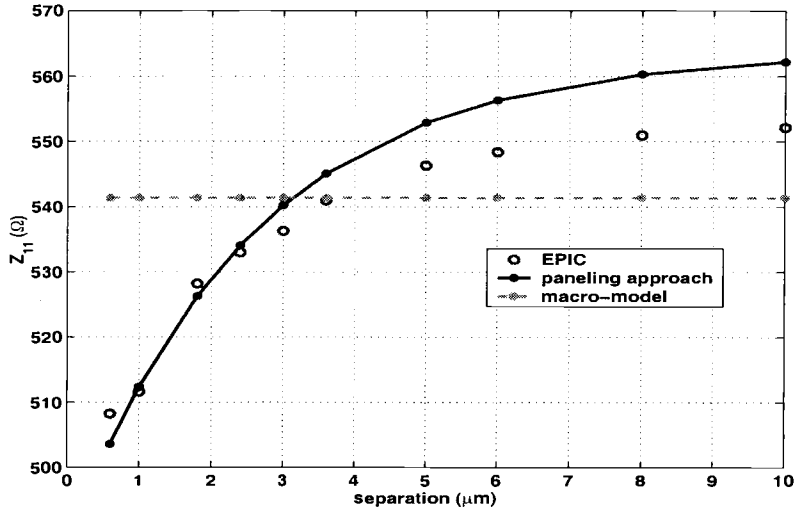

Figure 5.12. The variation of Z_{11} as the separation decreases for two $5\mu m \times 5\mu m$ contacts is predicted by the division of the contacts into panels. Each contact has been divided into 6 panels each.

There is, however, a difference between the actual values of Z_{ii} from EPIC and those predicted by this paneling approach. This is probably due to the error in calculating the Z_{ij} between panels that are adjacent to each other. Further analysis is required to find the correct expression for the Z_{ij} between adjacent panels.

5.7. Analysis of the mechanism of noise propagation in CMOS epitaxial substrates

Section 2.3 presented measurement results which proved that, as the separation between two ports is increased, the effect of R_{12} diminishes. This was concluded

from the fact that beyond a certain separation the parallel resistance, R_P, between the two identical ports approached the value of $2 \times R_{11}$. Hence, it was proposed that the (so-called) *critical separation* at which the parallel resistance becomes approximately equal to $2 \times R_{11}$ is the separation at which substrate noise coupling becomes predominantly a bulk phenomenon.

Simulations have shown that the approximate value for this *critical separation* is independent of the size of the contacts. It is a function of only the substrate layer thicknesses and resistivities.

The separation between two small ($0.85\mu m \times 0.7\mu m$) identical contacts is increased. The separation at which the ratio $\frac{R_P}{2R_{11}}$ becomes greater than 0.95 (i.e. the value of R_P is within 5 % of $2R_{11}$) is considered to be the *critical separation.* The above experiment is repeated for two large ($60\mu m \times 60\mu m$) contacts. The results for the above two cases are plotted in Figure 5.13. From Figure 5.13, it is seen that the *critical separation* lies approximately in the range of $15\mu m - 25\mu m$.

Despite the significant difference in size, the *critical separation* for either contact remains approximately the same, proving that this separation is independent of the size of the contacts.

The values of R_P and R_{11} used in Figure 5.13 were obtained for the profile shown in Figure 3.10. The same experiment was performed using the heavily doped substrate profile taken from [1]. This substrate profile has been reproduced in Figure 5.14. Figure 5.15 plots the values of $\frac{R_P}{2R_{11}}$ as a function of separation for the same two contact sizes as in Figure 5.13 for this profile. The *critical separation* in this case lies between $35\mu m - 45\mu m$, and as observed from simulations using the previous profile, is independent of the contact size. From the two cases presented

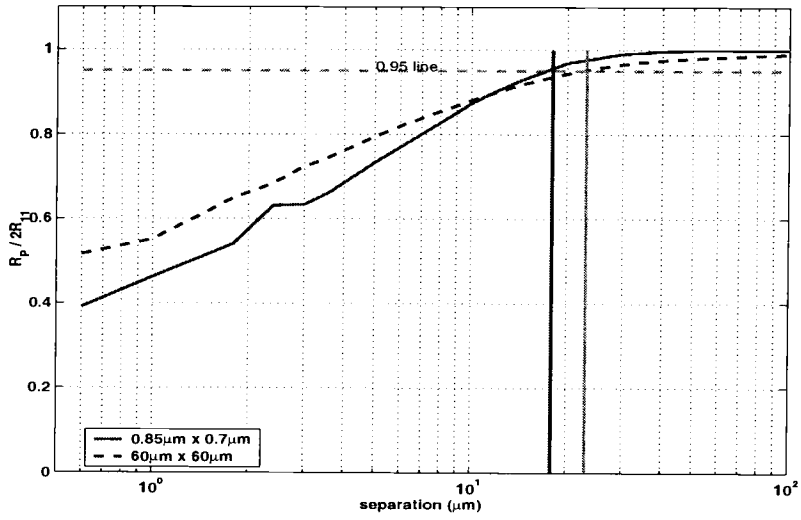

Figure 5.13. The range of separations at which $\frac{R_P}{2R_{11}}$ becomes greater than 0.95 is independent of contact size. The values have been obtained using the profile shown in Figure 3.10.

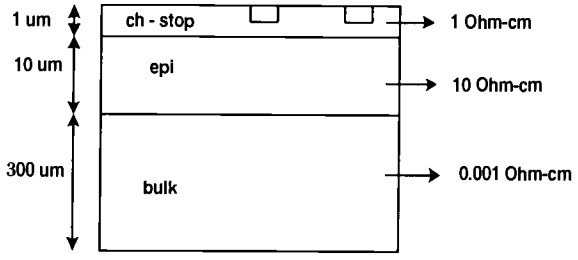

Figure 5.14. Profile of heavily doped substrate used to obtain the values of R_P and $2R_{11}$ in Figure 5.15.

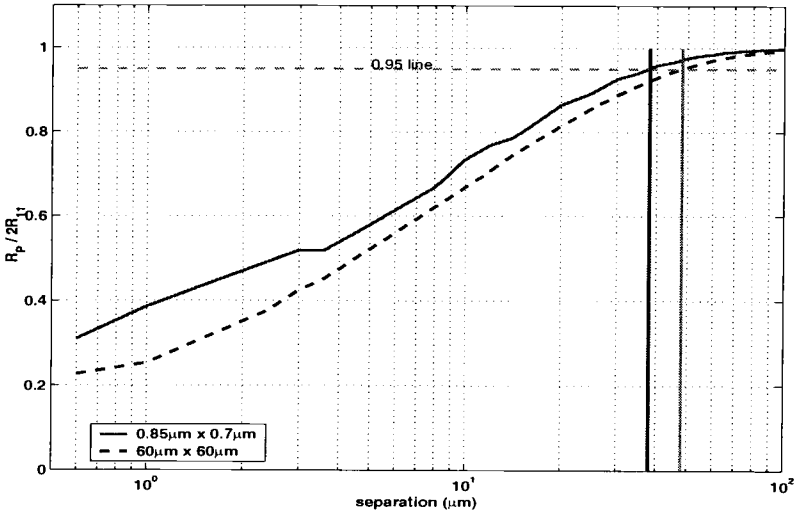

Figure 5.15. The range of separations at which $\frac{R_P}{2R_{11}}$ becomes greater than 0.95 is independent of contact size. The values have been obtained using the profile shown in Figure 5.14.

above, it can be concluded that the *critical separation* is a function of the substrate profile and is independent of contact size. This implies, that for a heavily doped substrate, the separation at which the effect of R_{12} can be neglected is independent of the sizes of the contacts.

This *critical separation* can be obtained by different means. For instance, Figure 5.16(a), plots the variation of the $\frac{R_P}{2R_{11}}$ that has been described above. Figures 5.16(b) and (c) plot the variation of $\frac{Z_{11}}{Z_{12}}$ and $\frac{Z_{11}}{Z_{11\,\infty}}$, respectively, as a function of separation. These curves have been plotted for two different contact sizes - $0.85\mu m \times 0.7\mu m$ and $60\mu m \times 60\mu m$. From Figure 5.16(b) it can seen that below a separation of about $15\mu m$, the ratio of Z_{11} to Z_{12} is independent of the size of the contacts. Beyond a separation of approximately $25\mu m$, this ratio depends significantly on the sizes of the contacts in consideration. Hence, for this substrate, it can be concluded that the *critical separation* lies between $15\mu m - 25\mu m$.

Finally, from Figure 5.16(c) similar inferences can be drawn about the *critical separation.* As can be seen, the ratio of $\frac{Z_{11}}{Z_{11\,\infty}}$ approaches 1 in the range of $15\mu m - 25\mu m$.

The results presented above provide insight to the mechanism of current propagation through heavily doped substrates. Additionally, the fact that the ratio of Z_{11} to Z_{12} is relatively independent of contact size, for separations lower than about $15\mu m$, can be used to model the variation of Z_{11} due to the proximity effect at these separations. These results can be used for better noise management in mixed-signal circuits.

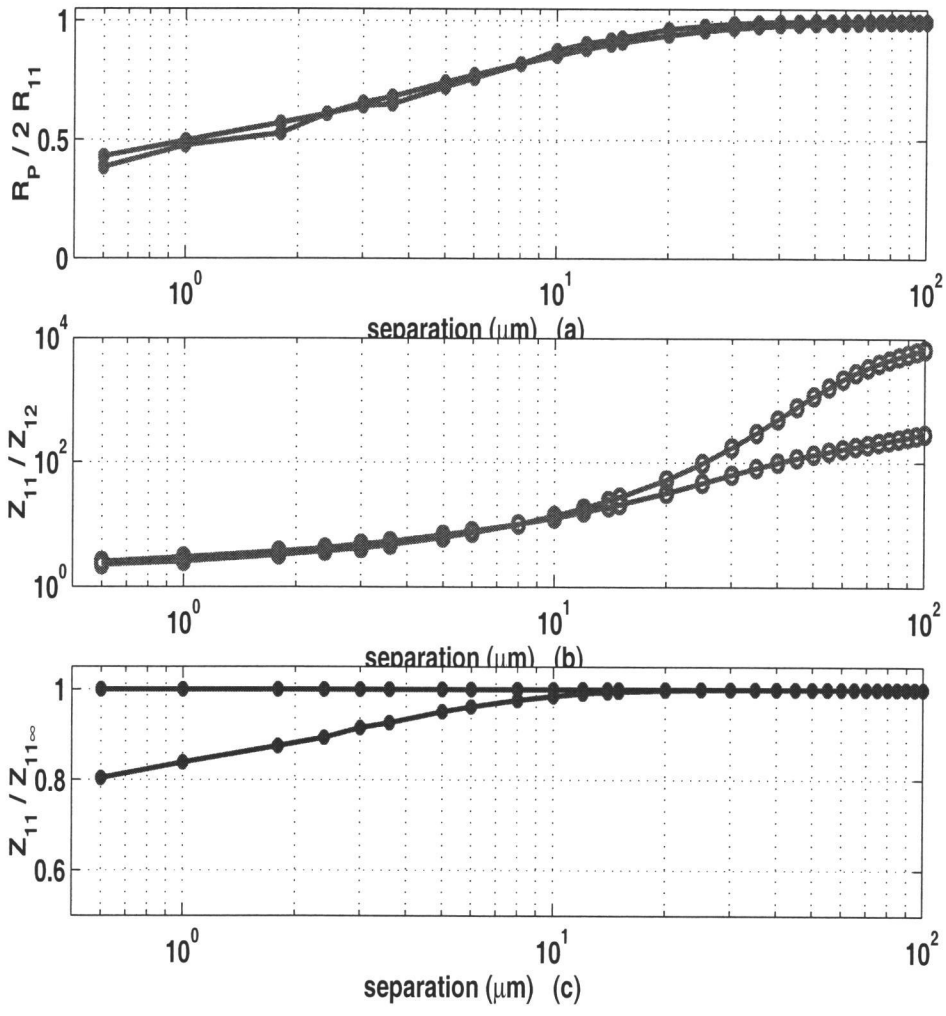

Figure 5.16. Plots of (a) $\frac{R_P}{2R_{11}}$ (b) $\frac{Z_{11}}{Z_{12}}$ and (c) $\frac{Z_{11}}{Z_{11\ \infty}}$ as a function of separation between two identical contacts. The contacts are $0.85\mu m \times 0.7\mu m$ and $60\mu m \times 60\mu m$. In (a) $\frac{R_P}{2R_{11}} \longrightarrow 1$, in (b) $\frac{Z_{11}}{Z_{12}}$ begins to diverge depending on contact size and finally in (c) $\frac{Z_{11}}{Z_{11\ \infty}} \longrightarrow 1$, all in the range of $15\mu m\ -\ 25\mu m$.

5.8. Summary

The above sections have shown that the z-parameter based macro-modeling approach is flexible and can be applied to a number of cases. Certain limitations of this approach have also been described. Possible solutions to these limitations have been proposed. These solutions involve the discretization of the contacts into panels. Heuristic guidelines for the use of the z-parameter based modeling have been presented as well.

6. CONCLUSION

6.1. Contributions

This thesis presents a comprehensive methodology and modeling approach for substrate noise coupling analysis in heavily doped CMOS processes. Guidelines for calibrating a 3-D simulator and a methodology to integrate this into a substrate network extraction program have been presented. An existing Z parameter based macro-model that is applicable to multiple contacts and is scalable with both the geometry and spacing of contacts has been enhanced and metrics for its performance have been described. Good agreement has been achieved between the model, simulations and measurements in terms of the percentage of noise coupling to a point of interest.

A Comprehensive Automated Substrate Parasitic Extraction Routine (CASPER) has been developed that enables the development of such scalable models. It automates calibration, data acquisition, curve fitting, verification and finally post processing. This will enable resources to be focussed on obtaining the correct expressions for substrate z-parameters and determining an efficient design of experiments for the test structures to be used in the curve-fitting.

The panel-based methodology that incorporates the z-parameter macro-model proves that it might be necessary to use different methodologies to obtain an accurate analysis of the digital switching noise that couples from the digital circuits to the sensitive analog circuits in large mixed-signal designs.

With this methodology the entire process of characterizing a substrate, extracting a scalable model and finally computation of substrate resistances can be

done orders of magnitude faster than existing approaches and without the dependence on extensive fabrication of test structures for the purpose - resulting in a reduction of both, cost and cycle time.

6.2. Suggested future research avenues

This thesis is part of an effort to develop a CAD tool that accurately and efficiently addresses the problem of substrate noise coupling. The CAD tool must be able to work from a layout and must be able to address the problem at a circuit level. It must also be able to provide a rough estimate of noise coupling before the actual full custom layout is in place.

Multiple software platforms have been used for the implementation of the various sections of CASPER. There is a stand-alone ANSI C calibration function (ORSTCAL). However, the curve-fitting engine for the model development has been developed in MATLAB. This must be implemented in C if future integration into a larger software environment is envisioned.

Further investigation on the relation of contact sizes to the mechanism of current propagation in the substrate will yield results that can significantly aid design decisions.

While the optimization routine and calibration procedure are complete in themselves and are automated already, the curve-fitting engine requires further automation.

First, a more efficient design of experiments (DOE) to determine the test structures for use in curve-fitting must be developed. The test structures that are

used to extract the parameters used in the expressions significantly affect the final values.

Second, the expressions used have been selected manually though a process of elimination and intuition. This particular step involves manual interference, to the otherwise almost completely automated CASPER set-up. One such method that may be feasible is to train a neural network to perform the "learning." A large database of possible functions can be set up and the neural network, as it progresses through its learning phase, can eliminate those functions that do not fit the data.

BIBLIOGRAPHY

[1] R. Gharpurey, "Modeling and analysis of substrate coupling in integrated circuits," Ph.D. Dissertation, University of California, Berkeley, 1995.

[2] N. K. Verghese and D. J. Allstot, "Computer-aided design considerations for mixed-signal coupling in RF integrated circuits," *IEEE Journal of Solid-State Circuits*, vol. 33, no. 3, pp. 314-323, March 1998.

[3] R. Gharpurey and R. G. Meyer, "Modeling and analysis of substrate coupling in integrated circuits," *IEEE Journal of Solid-State Circuits*, vol. 31, no. 3, pp. 344-352, March 1996.

[4] A. Samavedam, A. Sadate, K. Mayaram and T. S. Fiez, "A scalable substrate noise coupling model for design of mixed-signal IC's," *IEEE Journal of Solid-State Circuits,* vol. 35, pp. 895-903, June 2000.

[5] D. Ozis, T. Fiez, and K. Mayaram, "A comprehensive geometry-dependent macromodel for substrate noise coupling in heavily doped CMOS processes," *Proceedings of IEEE Custom Integrated Circuits Conference*, pp. 497-500, May 2002.

[6] A. J. van Genderen and N. P. van der Meijs and T. Smedes, "Fast computation of substrate resistances in large circuits," *Proc. European Design and Test Conference*, pp. 560-565, Paris, France, March, 1996.

[7] B. R. Stanisic, N. K. Verghese, R. A. Rutenbar, L. R. Carley and D. J. Allstot, "Addressing substrate coupling in mixed-mode IC's: simulations and power distribution synthesis," *IEEE Journal of Solid-State Circuits*, vol. 29, pp. 226-238, March 1994.

[8] I. L. Wemple and A. T. Yang, "Integrated circuit substrate coupling models based on Voronoi-Tessellation substrate macromodels," *IEEE Transactions on Computer-Aided Design,* pp. 1459-1469, Dec. 1995.

[9] C. G. Xu, "EPIC: A program for extraction of the resistance and capacitance of substrate with the Greens Function method," Department of ECE, Oregon State University, 2002.

[10] N. K. Verghese, T. J. Schmerbeck, and D. J. Allstot, *Simulation Techniques and Solutions for Mixed-Signal Coupling in Integrated Circuits*, Norwell, MA:Kluwer 1995.

[11] B. Owens, P. Birrer, S. Adluri, R. Shreeve, S. A. Arunachalam, H. Habal, S. Hsu, A. Sharma, K. Mayaram, and T. Fiez, "Strategies for simulation, measurement and suppression of digital noise in mixed-signal circuits," *Proceedings of IEEE Custom Integrated Circuits Conference*, 2003 (to appear).

[12] D. Ozis, K. Mayaram, and T. Fiez, "An efficient modeling approach for substrate noise coupling analysis," *ISCAS 2002*, vol. 5, pp. 237-240, May 2002.

[13] D. Ozis, "An efficient modeling approach for substrate noise coupling analysis with multiple contacts in heavily doped CMOS processes," M. S. Thesis, Oregon State University, August 2001.

[14] R. C. Jaeger, *Introduction to Microelectronic Fabrication*, 2e, Purdue Modular series on solid state devices, Prentice-Hall 2002.

[15] MATLAB 5.1 help, Introduction to Algorithms, The MathWorks, Inc., 2001.

[16] CADENCE, Substrate Coupling Analysis User Guide, Product Version 4.4.6, April 2001.

[17] Agilent Technologies, Agilent 4156B Precision Semiconductor Parameter Analyzer User's Guide - General Information, vol. I, Edition 4, May 2000.

[18] CADENCE, Dop2sti User Guide, Product Version 4.4.6, April 2001.

[19] D. K. Su, M. J. Loinaz, S. Masui and B. A. Wooley, "Experimental results and modeling techniques for substrate noise in mixed-signal integrated circuits," *IEEE Journal of Solid-State Circuits*, vol. 28, pp. 420-430, April 1993.

[20] E. Yamashita, "Variational method for the analysis of microstrip-like transmission line," *IEEE Trans. Microwave Theory and techniques*, pp. 529-535, August 1968.

[21] N. K. Verghese, "Extraction and simulation techniques for substrate coupled noise in mixed signal integrated circuits," Ph.D. Dissertation, Carnegie Mellon University, August 1995.

[22] P. Milliozi, L. Carloni, and A. Sangiovanni-Vincentelli, "Subwave: a methodology for modeling digital substrate noise injection in mixed-signal IC's," *Proceedings of IEEE Custom Integrated Circuits Conference*, pp. 385-388, May 1999.

APPENDICES

APPENDIX A. ANSI C Calibration Routine

A short description of the ANSI C implementation of the Calibration routine is presented.

1. ORSTCAL is a stand-alone ANSI C application that can be compiled either on a Solaris or HP Workstation.

2. It has an interface to EPIC.

3. The user needs to input only the reference values of the calibration metric (Z_{11} for different contact sizes in a heavily doped substrate) and the initial values for the substrate layer resistivities and thicknesses. This must be done in the file *main.c*. The contact sizes and separations between the contacts must be listed in a file that is defined by the pre-processor macro CALIBSTRS. The default file name is *cal_data.dat*.

4. Suitable options for the optimization can be set in the header file *options.h*. Machine specific options must be set in the file *mconf.h*.

5. The default options that have been set, yield results comparable to the initial MATLAB implementation of the same calibration routine.

6. A Makefile has been created which when executed creates an executable called ORSTCAL. Additional information about program specifics have been provided in the documentation accompanying the package.

7. To run the application type *orstcal* at the command prompt.

APPENDIX B. Measurement structures on Test Chip

The test structures that were fabricated on the test chip in the TSMC $0.35\mu m$ CMOS epitaxial process are listed below.

1. Arrays of $0.85\mu m \times 0.7\mu m$, $0.85\mu m \times 1.5\mu m$ and $0.85\mu m \times 3.1\mu m$ contacts for measuring Z_{12} at small separations.

2. Arrays of $2.4\mu m \times 2.4\mu m$, $4\mu m \times 4\mu m$, $6\mu m \times 6\mu m$ and $10\mu m \times 10\mu m$ contacts at separations of 10, 25, 40 and 50 μm.

3. Arrays of $10\mu m \times 30\mu m$, $20\mu m \times 40\mu m$,contacts at separations of 10, 25, 40 and 50 μm.

4. Three $40\mu m \times 40\mu m$ contacts at separations of 10, 25, and 50 μm.

5. Two $60\mu m \times 60\mu m$ contacts at separations of 10 and $25\mu m$.

APPENDIX C. De-embedding the Back-plane to Die-perimeter ring resistance

The figure below shows the resistance between the actual back-plane and the die-perimeter ring contact. Also shown in the figure are the resistances between the injector and the die-perimeter ring and between the sensor and the die-perimeter ring.

The resistance R_{BP_DP} between the die-perimeter ring and the back-plane is in reality the R_{ii} of the die-perimeter ring. A guard ring can be considered to be like any other contact that has been discussed so far - only different in shape. From Chapter 4 it is seen that Z_{11} of a contact decreases with increasing size. Hence, the die-perimeter ring in the die will have a very low self-resistance.

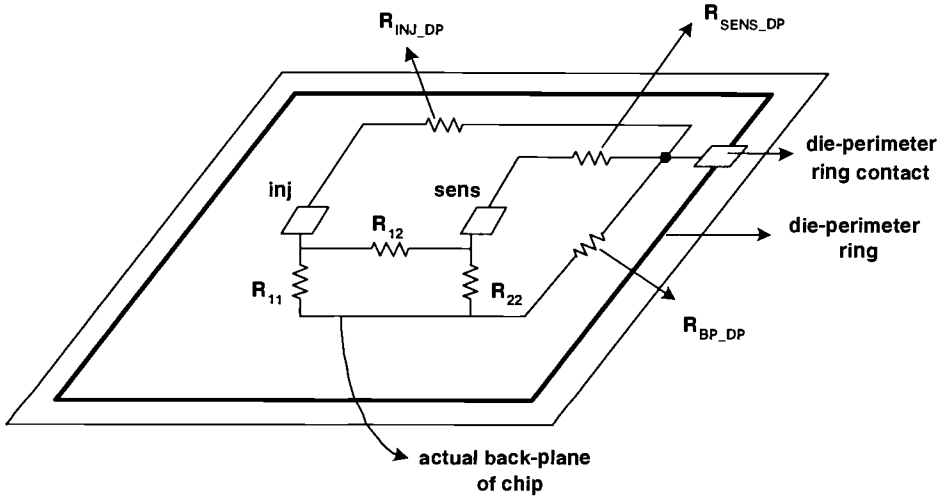

The procedure to de-embed the back-plane to the die-perimeter ring resistance is shown below. The various currents and voltages are explained in the following figure. The known quantities (from measurements) are:V_F, etc.

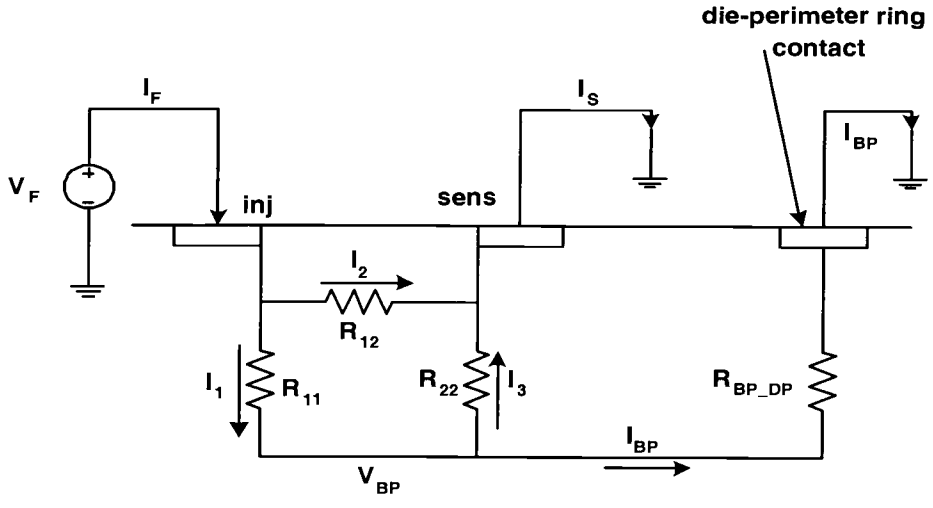

$$I_F = I_1 + I_2 \tag{C1}$$

$$I_S = I_2 + I_3 \tag{C2}$$

$$I_1 = I_{BP} + I_3 \tag{C3}$$

But $R_{22} \gg R_{BP\_DP}$. This implies that $I_3 \ll I_{BP}$. From measurements, it is seen that I_3 is at least a couple of orders of magnitude smaller than I_{BP}. Hence, Eq. (C3) can be approximated as

$$I_1 \approx I_{BP} \tag{C4}$$

R_{11} must be obtained as

$$R_{11} = \frac{V_F - V_{BP}}{I_1} \tag{C5}$$

But using the approximation of Eq. (C4),

$$R_{11} = \frac{V_F - V_{BP}}{I_{BP}} \tag{C6}$$

R_{12}, the cross resistance between the injector and the sensor must be calculated as follows:

$$R_{12} = \frac{V_F - V_S}{I_2} = \frac{V_F - 0}{I_F - I_1} = \frac{V_F}{I_F - \frac{V_F - V_{BP}}{R_{11}}} \tag{C7}$$

or

$$R_{12} = \frac{V_F R_{11}}{R_{11} I_F - V_F + V_{BP}} \tag{C8}$$

Note that Eqs. (C6) and (C8) correspond to Eqs. (2.18) and (2.19), respectively.

APPENDIX D. Test Structures used to Fit Expressions for m_1, m_2, m_3, m_4 and m_5

As described in Chapter 4, Section 4.3.3, the expression for Z_{12} as a function of x requires three parameters, m_1, m_2 and m_3, which are a function of contact dimensions. The table below lists the contact numbers and corresponding contact sizes used to fit expressions for m_1, m_2 and m_3 in Figure 4.10.

Contact Number	*Contact Size* ($\mu m \times \mu m$)
1	1×1
2	1×3
3	1.5×1.5
4	1×4
5	2×2
6	2.4×2.4
7	2×5
8	3.1×3.1
9	3×5
10	3.5×3.5
11	4×5
12	6×6

As described in Chapter 4, Section 4.3.4, the expression for Z_{12} as a function of y requires two parameters, m_4 and m_5, which are functions of contact dimensions. The table below lists the contact numbers and corresponding contact sizes used to fit expressions for m_4 and m_5 in Figure 4.14.

Contact Number	*Contact Size* ($\mu m \times \mu m$)
1	0.85×0.7
2	0.85×1.5
3	0.85×3.1
4	1×1
5	1×2
6	1.5×1.5
7	2×2
8	2.4×2.4
9	2×4
10	3.1×3.1
11	5×5
12	6×6